THESIS

DEVELOPMENT OF A METHANE CAVITY RING-DOWN SPECTROMETER FOR DEPLOYMENT ON GROUND AND AERIAL BASED VEHICLES

Submitted by:

Benjamin Martinez Jr.

Department of Mechanical Engineering

In partial fulfilment of the requirements

For the Degree of Master of Science

Colorado State University

Fort Collins, Colorado

Spring 2020

Master's Committee:

Advisor: Azer P. Yalin

Dylan Yost
Bret Windom

ABSTRACT

DEVELOPMENT OF METHANE CAVITY RING-DOWN SPECTROMETER FOR DEPLOYMENT ON GROUND AND AERIAL BASED VEHICLES

Recent findings show that the oil and natural gas industry is responsible for a large portion of total anthropogenic methane (CH_4) emissions. These findings have driven the need for suitable methane detection and quantification methods. Methane emissions on the scale that the oil and gas industry produce (13 Tg[CH_4]/year) can cause environmental effects comparable to that of CO_2 due to methane's high global warming potential. The present thesis focuses on continued developments and improvements to a laser-based methane sensor that uses the open-path cavity ring-down spectroscopy (CRDS) technique. The sensor is intended for continuous mobile monitoring of methane emissions from the oil and gas industry by deployment on ground and aerial based vehicles.

Sensor performance in a range of environmental conditions is characterized and shows the feasibility of deploying the sensor in real world applications. Indoor accuracy tests were done utilizing a closed-path system and verified through comparison with a commercial analyzer. Sensor measurements compared to the commercial analyzer showed good 1:1 agreement. Allan variance studies within laboratory measurements demonstrated the sensor's high sensitivity of ~10 ppb. A heater system was designed and implemented for overall improvement in low temperature conditions. The heater system successfully improved the thermal range of the sensor to temperatures as low as 0°C. Environmental tests also showed the sensor's reliability in harsh winter conditions over a ~70-day period of continuous measurement. The sensor's methane

plume detection ability and sensitivity in simulated controlled releases through vehicle deployment is demonstrated and good 1:1 agreement was found comparing against a commercial analyzer in the field. Controlled release experiments demonstrated CH_4 measurements more than 400 meters away from the source at an emission rate of 0.5 g[CH_4]/s. A retro-fitted closed-path cell was constructed and tested in field campaigns to reduce noise due to Mie scattering. Additional field testing with simulated controlled releases were performed to test a modified, lightweight (4.1 kg) sensor mounted on two unmanned aerial vehicle platforms. Detection of various plumes in the UAV configuration was shown to be feasible with the current mounting method. Sensitivity in UAV flights were as low as 17 ppb which demonstrated the robust opto-mechanical capabilities of the sensor.

ACKNOWLEDGMENTS

I first want to thank my advisor, Professor Azer Yalin, for his continued support throughout my time at CSU. I also want to express my gratitude for his research guidance and for allowing me to join his group that has provided me with an amazing cohort of extremely intelligent and capable people. Thank you to Laurie McHale who mentored me and prepared me for this research. Thank you to Soran Shadman, Adam Friss, Betsy Farris, Charles Rose, and Simon Gaßner who all offered their vast knowledge throughout my time in this group. I would also like to thank Carter (Kobo) Butte, Thaddeus (The Robot) Wegner, and James (Sipich) Sipich for keeping me sane through ample rounds of darts and distracting me while writing this thesis. I also want to thank AJ (Puuugaaa) Puga for coming on the project and helping me set up my experiments at Christman Field. Thank you also to Collin VanTilburg, Jared Ham, and Dr. Frederick Smith for their continued support on the UAV system. I am also grateful for the assistance of Arsineh Hecobian on the use of a Picarro sensor which she also graciously allowed us to use. Thanks also to Tom Miller who has helped with the electronics of the sensor since the beginning of this project. A huge thank you goes out to my family and my girlfriend's family for continually supporting me through all of my education even though they most of the time had no idea what I was doing. Lastly, I would love to thank my beautiful girlfriend, Meg Strauss, for always being there for me even when I didn't know I needed it. I would have never gotten through this program and thesis without her love and support and amazing editing knowledge.

TABLE OF CONTENTS

LIST OF TABLES

LIST OF FIGURES

CHAPTER 1: Introduction

1.1 Background and Motivation: Methane Emissions from Oil and Gas

The precise detection and quantification of anthropogenic hydrocarbon emissions that produce harmful effects to the environment is currently a topic that has garnered extreme interest in the scientific community. Anthropogenic emissions of greenhouse gases (GHG) are at an all-time high according to an International Intergovernmental Panel on Climate Change (IPCC) report published in 2014[1]. Methane, with chemical formula CH_4, has become one of the pivotal hydrocarbons being researched today because of its recent and continued rise in global background concentration.

Methane is a naturally occurring tropospheric gas with a moderate lifetime of 12.4 years in the atmosphere[1]. The importance in monitoring the increase in worldwide methane is due to two factors:

1. Methane's extreme potency as a greenhouse gas which is directly affecting global climate
2. Methane's ability to indirectly contribute to global climate change and pollution through the formation of ozone and water vapor.

CH_4 creates water vapor and tropospheric ozone by photochemically reacting with nitrogen oxides[2]. Ozone in the lower atmosphere is a pollutant that is harmful if inhaled, affects vegetation, and can cause vision impairment[3]. Water vapor functions as greenhouse gas in the upper atmosphere, which can produce positive feedback loops[2].

Methane's potency as a greenhouse gas can best be understood when comparing its global warming potential (GWP) to that of CO_2. GWP is the weight assigned to climate forcing

agents in relation to CO_2 over a set amount of time in the atmosphere[1]. Over a span of 20 years, CH_4 has a global warming potential 84 times that of CO_2[1]. In 2010, CH_4 accounted for 16% of the total anthropogenic GHG emissions. Out of all of the greenhouse gases, anthropogenic CH_4 has the second highest radiative forcing term[2] of 0.97 Wm^{-2} as compared to that of the highest GHG, CO_2, which is 1.7 Wm^{-2}. Its steady increase since the industrial revolution raises concerns over the overproduction of methane caused primarily by anthropogenic sources[1]. The global background concentration of CH_4 is currently around 1.8 ppm, which has increased 164 percent since 1750[4].

While methane does have an abundant number of natural sources that release it into the lower atmosphere, such as wildfires, permafrost, and livestock, they are notably difficult to mitigate[1]. The accurate quantification of methane released into the troposphere by anthropogenic sources has not yet been completed but is clearly incredibly important in understanding the steady increase of atmospheric methane over time. There are varying estimates from the scientific community for CH_4 emissions which range from 542 to 852 Tg[CH_4] per year[2]. Disagreement among published estimates leads to the need for better characterization of emission rates[5]. It is estimated that 50-65% of total methane released into the troposphere is anthropogenic[6], but there is still much uncertainty in these estimates because of a lack of accurate detection methods.

One of the main anthropogenic sources of methane emissions today is the oil and natural gas industry. The main component of natural gas is methane which comprises generally ~87-97% of natural gas[7] by mass fraction. Recent years in the United States have seen a movement to try and reduce overall greenhouse gas emissions, specifically that of CO_2, by using natural gas as a “bridge fuel” to renewables. Natural gas produces only half as much CO_2 as coal per unit of

combustion products which makes it desirable as a low emission fuel source[8]. While many claim methane as a "clean fuel" because of its low CO_2 emissions when combusted, it is important to note that if not burned, methane causes harmful effects when released into the atmosphere. Fugitive emissions of methane could lead to climate effects equivalent, if not worse than those produced by CO_2 emissions; therefore, excess emissions of methane produced during extraction and transportation in oil and gas facilities could negate the benefits produced by switching to natural gas the first place.

The natural gas industry currently has the largest production increase estimate of all fossil fuel industries[9]. This increase is partly due to its lower GHG emissions, but is also due to low cost, abundance, and versatility[9]. Large resources of natural gas from shale formations are abundant in the United States[9]. This abundance has led to a surge of hydraulic fracturing which has contributed at least 40% of total natural gas production in the United States since 2012[6]. Some studies estimate shale-gas production in North America accounts for more than half of all of increased emissions from fossil fuels globally[10]. There are also enormous methane reserves beneath artic permafrost which are estimated to be 53% of all fossil fuel reserves on Earth[8]. Taping into these reserves could produce an enormous energy source, but also has the potential to be an incredibly large emission source.

The rise in use of natural gas has increased the need to quantify the amount of CH_4 being released by the natural gas industry. In Colorado there has been an increase from 33,815 wells in 2007 to over 53,000 in 2019[11]. The U.S. Energy Information Administration's (EIA) national oil and gas well count estimates that there were 997,000 total producing wells in the United States in 2017. Natural gas production is the second largest source of anthropogenic CH_4 emissions[4]. Recent advancements in extracting methods have also led to easier access to reserves.

Advancements in extracting methods leads to facilities being closer to populated areas which can cause pollution issues to the public through the production of tropospheric ozone. Outside of the effects that CH_4 can have on the climate and environment, its quantification is also a priority to oil and gas companies since it is a direct loss of product and worldwide environmental regulation requirements have been established. According to a study done by the Environmental Defense Fund, approximately $2 billion a year is lost by the oil and gas industry through methane leakage[5]; therefore, active quantification of methane losses from oil and gas facilities is incredibly important.

1.2 Approaches for Methane Detection

Due to current concerns over fugitive emissions from oil and gas facilities, a multitude of methods for methane detection have been under development by academia and industry. The Oil and Gas Climate Initiative (OGCI), a company led initiative taking steps towards the prevention of climate change, has focused heavily on the cooperative effort to reduce methane emissions from oil and gas infrastructure. Companies such as BP and ExxonMobil, express a goal to "reduce the collective average methane intensity of our aggregated upstream gas and oil operations[12]." The following section gives an overview of current commercial and academic technologies used to detect methane for the oil and gas industry.

Quantitative measurements of methane over a range of spatial scales are needed to help quantify and reduce methane emissions from oil and gas extraction sites. There are currently various methods for quantitative and qualitative detection of methane. On larger spatial scales high altitude planes are equipped with a variety of sensors capable of detecting methane from high altitudes over areas of interests[13,14]. An airborne methane plume spectrometer (AMPS) uses visible infrared imaging spectroscopy to detect methane to high accuracy from a 100-meter flight

altitude[15]. Other high-altitude methods include HyTES, a hyperspectral thermal emission spectrometer that takes thermal IR radiance measurements at 1 km height[16,17]. Satellite systems such as MethaneSAT[18] are also being developed to measure methane on 1x1 km or 2x2 km spatial resolution[19]. Airborne measurements have the ability to cover large areas and can be used to verify plume measurements through coordination with ground-based sensors making in situ measurements[15–17].

On smaller spatial scales, infrared cameras and laser-based sensors are at the head of the helm for methane detection. The current standard used in industry to detect methane is optical gas imaging (OGI) cameras[20]. OGI cameras are infrared/thermal cameras designed specifically for the observing of gas by producing an image of radiation intensity. OGI cameras use quantum detectors requiring cooling down to ~-203℃ which allow for the reduction of electrons in the valence band[21]. When the material is exposed to incoming radiation, the radiation transfers enough energy to bump electrons into the conduction band creating a photocurrent proportional to the intensity of the radiation. A filter is also used to narrow the band pass. A gas plume can be imaged when it absorbs radiation in the band pass range which reduces the overall amount of radiation striking the detector[21].

Several papers have been written describing the effectiveness of OGI cameras[13,20]. While OGI cameras are effective in visualizing the plume's location, they come with a variety of downsides. One such downside is the issue of reviewing all the footage that is produced by the cameras. Large data sets encourages individual inspection of wells rather than surveillance over long periods of time and large area[5,20]. Other issues include the requirement of short imaging distances to verify a leakage and a high dependence from environmental conditions (e.g. temperature and wind conditions) on detection effectiveness[13]. Other studies have found that

OGI cameras are "good enough" at detecting small methane leaks, but only at relatively short distances[20]. Monitoring large areas would require a lot of manpower and individual inspections. Most OGI cameras are also not quantitative in their measurements.

Laser based methods for detecting trace gases and methane are also common. Picarro sensors utilize closed-path cavity ring-down spectroscopy (described in more detail below) to measure various trace gases in the atmosphere[22]. Open-path laser spectroscopy (OPLS)[23] using a Herriot Cell has also been used to create a lightweight, highly sensitive in-situ methane measurement instrument. The instrument was primarily designed for use on an unmanned aerial vehicle (UAV) and therefore is extremely lightweight (250 g) and low power (<8 W). The OPLS sensor also has high sensitivity (10 ppb at 1 second averaging time). Wavelength modulation spectroscopy (WMS) has also been utilized to measure vertical methane gradients by mounting on an unmanned aerial system[24]. This WMS sensor is also lightweight (1.6 kg) with high sensitivity (10 ppb at 1 second averaging time) but requires ground-based reference when calculating concentration.

1.3 Design Overview of CRDS Open-Path Sensor

The sensor described in this work uses a cavity enhanced absorption technique called cavity ring-down spectroscopy (CRDS) which allows extremely sensitive detection of methane. Four iterations (Phase I – Phase IV) of this methane sensor have been developed. The design and development of the sensor through Phase III was primarily done by Dr. Laura McHale, a recent Ph.D. graduate from our research group. McHale's contributions to this work include the design of the sensor's opto-mechanical structure, the data acquisition and initial fitting algorithms, the main electronic components, as well as preliminary testing of various aspects of Phase III sensor's performance[25].

The work presented in this thesis outlines the continued, comprehensive testing and development of Phase IV of the sensor. Chapter 2 describes tests and analysis of the sensor's accuracy and precision as well as improvements made to the sensor's hardware and software. Chapter 3 and Chapter 4 outline the detailed testing of sensor integration on ground and aerial vehicles (e.g. fixed wing and rotor-style UAVs). Sensor performance (e.g. accuracy, precision, detection ability) is examined through all platforms. Development and testing of mechanical variations of the mobile sensor are also described in Chapter 3.

Our goal with this methane sensor is to offer the spatial resolution (<10 m) for localization and quantification[26] of emissions from individual sites (e.g. wells) through a mobile ground vehicle or UAV mounted sensing approach. Mobile sampling can provide a scalable approach toward quantification of methane emissions. For example, sensors mounted on company work vehicles can continuously monitor emissions on a daily basis.

While there are already commercial methane sensors that employ CRDS, our work focuses on the use of an open-path design where air flows through the open cavity. Open-path configurations allow for faster temporal response with high sensitivity (10-15 ppb at 1 second averaging times), while also having low power consumption (<30 W) and overall mass (~4.1 kg). Sensitivity, time response, and accuracy are all needed to accurately capture methane plumes. The sample rate of the sensor in this work is one measurement per second which allows for accurate retrieval of plumes. The low power consumption and weight not only makes the sensor less complex, but it also offers a more suited design for vehicles and UAV integration.

Closed-path configurations require vacuum pumps to pump the sample within a cell. Closed-path configurations reduce the time response due to air flow lag while also distorting the signal through temporal broadening. The cell utilized in closed-path configurations is primarily

used to reduce and fix the pressure to narrow the spectral lines and precisely control the temperature for more accurate retrieval of concentration. Our open-path configuration allows ambient air to flow through the cavity in real-time allowing faster time response; however, it requires ambient temperature and pressure data to infer concentration (see Equation 1.2). Open-path also reduces the need for a vacuum pump or controlled cavity cell, allowing for vehicle integration, low power, and vehicle mobility. Closed-path cells are also able to reduce influence in measurements due to other phenomena such as Mie scatter. This is done by filtering the air sample introduced into the cavity. Current and past work done by our group has shown that various methods can be used to maintain adequate sensitivity in the field (10-20 ppb at 1 second averaging times) even when employing an open-path configuration[25,27].

Figure 1.1 shows a full model of the truck mounted configuration for the open-path sensor. The optical head where the air sample is measured within a high-finesse cavity has approximate dimensions of 84 cm x 18 cm x 15 cm, with as mass of ~3.3 kg. The electronics enclosure (i.e., the module containing the micro-controller, circuit boards etc.) has approximate dimensions of 40 cm x 40 cm x 15 cm and a mass of ~22 kg (excluding the roof-rack mount). The current sensor being developed in this thesis is the fourth iteration (Phase IV) of the sensor which has been modified from previous work. A much smaller, compact package developed for UAV mounting (Phase III) is described in Chapter 4.

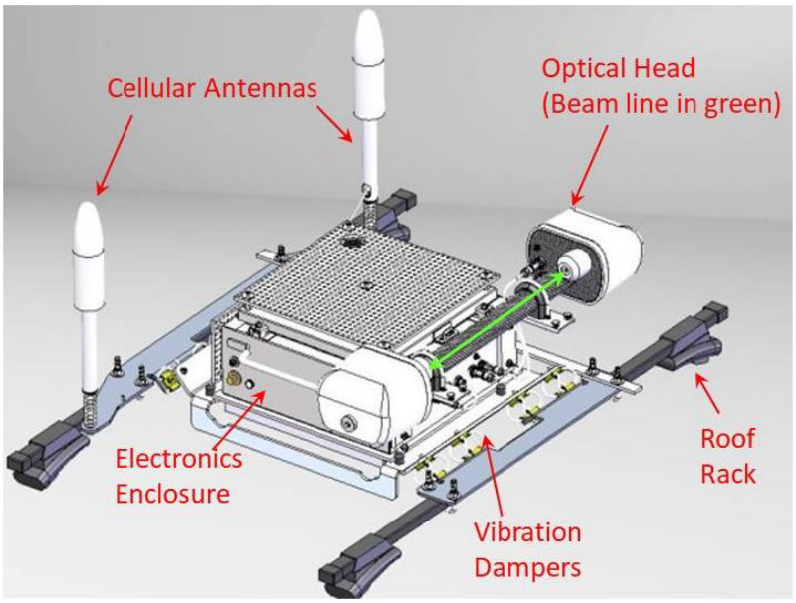

Figure 1.1: CAD model of sensor as deployed on automobile roof [27].

1.3.1 Sensor Opto-Electronics

Figure 1.2 shows a schematic of the main opto-electronic aspects of the sensor. The laser source is a continuous-wave distributed feedback (DFB) diode laser (NEL/NTT) in a 14-pin butterfly package. The laser wavelength is ~1651 nm. Recording of the spectrum is done by current-scanning the laser through the use of a compact (OEM-type) controller. A thermo-electric cooler (TEC) is used to fix the laser temperature to allow accurate current-scanning over a specific spectral region. An inline fiber isolator prevents back reflections from the cavity to the laser which is then followed by a fiber coupled acousto-optic modulator (AOM). The AOM (Gooch & Housego, T-M040-0.5C8J-3-F2S) functions as an optical switch with fast response to deflect the laser away from the cavity (thus allowing for ring-down measurements). Light exiting the final fiber after the AOM is approximately 5 mW in power and is passed to free space through an adjustable focus aspheric FC collimator (Thorlabs CFC-8X-C). The collimator is adjusted to achieve spatial mode matching to the optical cavity.

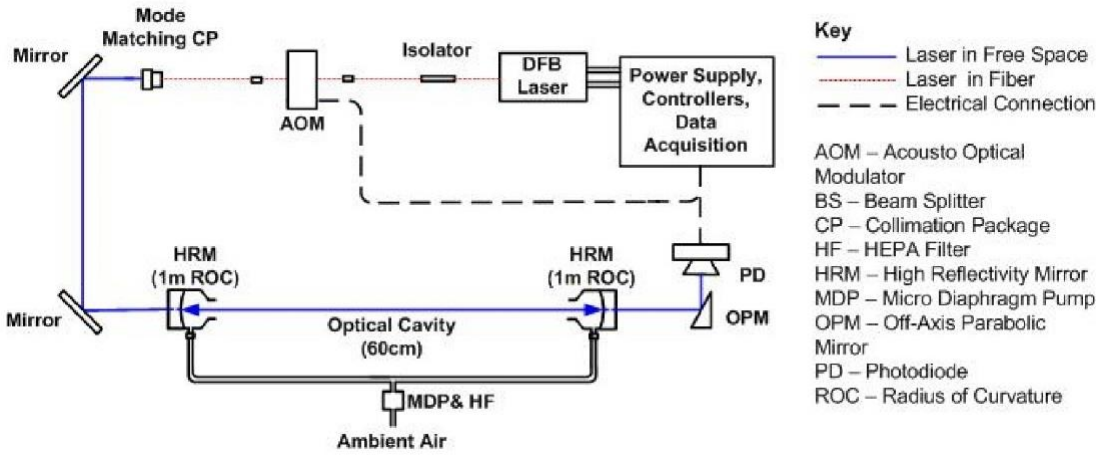

Figure 1.2: Schematic diagram of CRDS methane sensor.

In free space, two steering mirrors are used to propagate the beam through one side of the resonant optical cavity. The cavity is characterized by two high reflectivity (HR) mirrors (Advanced Thin Films) separated by 60 cm. The HR mirrors have dielectric coatings on fused silica substrates and have reflectivity of R~0.99994 at 1651 nm. Light is then coupled out of the cavity through an off-axis parabolic mirror to a high-gain low-noise InGaAs photodetector amplifier module (Analog Modules, 712B-4-DC). TCB Engineers developed the data acquisition system for the sensor which utilizes a National Instruments sbRIO-9651 for logic and control. Acquisition, triggering, and laser scanning are implemented on the FPGA side of the sbRIO.

The laser is continuously scanned (1-10 Hz) across the range of interest (1650.89 nm to 1651.03 nm) containing a methane absorption feature. Each passage across a cavity resonance a trigger circuit turns off the AOM voltage to deflect the beam away from the cavity allowing for a ring-down measurement[28]. At the moment a resonance voltage signal at the photodiode detector exceeds a set threshold trigger value, the software turns off the 3.3 volt signal to the AOM to directing further incoming light away from the cavity. The light within the cavity then decays (ring-down signal) as a function of absorption and is fit to a linearized exponential by an iterative nonlinear least squares method. The measured ringdown's are converted into optical absorption

values $k(\nu)$ and the relative-frequency axis is set by etalon calibrations to yield the absorption spectrum. The ring-down ingestion rate (i.e. the number of ring-downs measured per second) varies according to threshold trigger values but is generally set to ~500 τ/s. Phase IV sensor software design incorporated an algorithm which varied the threshold trigger level according to averaged ingestion rate in order to remain at a set ingestion rate over periods where slight misalignments may occur (e.g. thermal effects). More specific detail can be found in our groups previous publications[25,29].

1.3.2 Spectral Simulations

The species concentration is found by converting ring-down times, τ, into absorption coefficients, $k(\nu)$. The spectral region where the laser is swept has four contributing methane absorption lines that sum to form a single feature at atmospheric pressure. A simulation of this absorption spectrum can be seen in Figure 1.3.

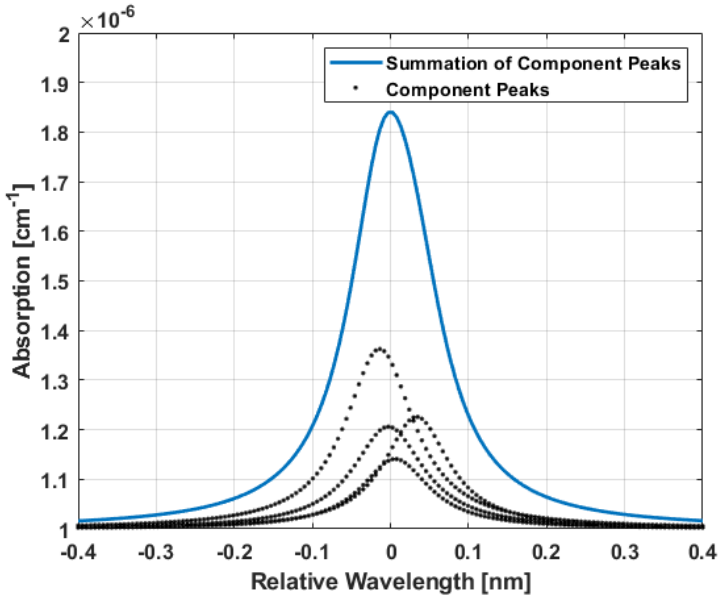

Figure 1.3: Simulated absorption in spectral region where sensor laser wavelength is scanned. T =300 K, P=0.84 atm, [CH_4] = 2.0 ppm. Dotted lines show the four contributing methane peaks used in the synthetic spectrum while the blue line denotes the summation.

Under atmospheric conditions, due to relative high pressure (~1 atm), Doppler broadening is negligible; therefore, the four component lines can be modeled using only Lorentzian line shapes[30]. A summation over the four contributing Lorentzian absorption lines can be used to simulate the spectrum (and fit for concentration). The equation for the synthetic spectrum is given as:

$$k(v) = b + \sum_{i=1}^{4} \varphi_L(v, v_{0i}, \Delta v_i) P S_i n_i \tag{1.1}$$

$$k(v) = b + \left(\frac{1}{\pi}\right)\frac{P^2}{T}[CH_4] \sum_{i=1}^{peaks} \frac{S_i C_i}{(v - v_0 + v_{0i})^2 + (P * C_i)^2} \tag{1.2}$$

Where the cavity baseline loss is given by b, and the index i denotes the summation over the four lines. The frequency-normalized Lorentzian line shapes are given by φ_L, where v_{0i} is the center frequency, the pressure broadening terms are given by C_i, and Δv_i is the width. Both frequency center and width were determined from HITRAN simulations[25]. The line strengths, S_i, are also determined from HITRAN simulations. P is the pressure, T is the temperature, and n_i is the species concentration. Fitting requires knowledge of ambient temperature and pressure and are recorded with two integrated sensors taking real time measurements (Omega RTD-806 and Honeywell PX2AM1XX001BAAAX respectively). The region scanned is a range from 1650.89 nm to 1651.03 nm (air wavelengths). Equation 1.2 is used to fit CRDS measurements to retrieve concentration values. Three free fit-parameters, the baseline loss (corresponding to mirror reflectivity), the laser frequency offset, and concentration are used to fit the spectrum.

1.4 Theory

Cavity Ring-Down Spectroscopy (CRDS) is an optical based spectroscopic technique that measures optical extinction by light-matter interactions, namely the scattering and absorbing of

light. It functions based on two concepts: absorption spectroscopy and the increase of interaction times through resonant optical cavities.

1.4.1 Spectroscopy

Spectroscopy is a branch of physics that deals with the absorption and emission spectra that are produced when electromagnetic radiation interacts with matter. As quantum mechanics describes, atoms and molecules exist only in specific quantum states that have quantized energy and angular momentum[31]. The total internal energy is stored as a sum of rotational, vibrational, and electronic modes. Due to energies being quantized, discrete differences in energies exist between molecule quantum states. These discrete differences are exploited in spectroscopy. Emission and absorption of photons produce changes in energy which correspond directly with these state transitions[31].

The basis of cavity ring-down spectroscopy relies on absorption characteristics of different molecules. Absorption occurs when a molecule or atom changes quantum states from lower to higher energy due to the absorption of a photon[31]. Planck's Law, Equation 1.3, describes the photon energy relation to a quantum state transition that occurs during absorption.

$$\Delta E = E_{upper} - E_{lower} = h\nu = h\frac{c}{\lambda} \tag{1.3}$$

Where the energy stored within the photon is denoted as ΔE, E_{upper} and E_{lower} are the energies of the upper quantum state and lower quantum states respectively, h is Planck's constant, and ν is the frequency of the electromagnetic wave. The total change in internal energy of a molecule corresponds with the sum of the individual changes in rotational, vibrational, and electronic energy[31].

When plotting absorption of a specific atom or molecule versus frequency, one will find discrete "lines" which correspond to the allowed differences in energy between transitions. These lines are often thought of as delta functions; but, due to natural and collisional broadening effects caused by temperature and pressure, the lines have finite spectral widths and profiles referred to as "lineshapes". The lineshape relates to specific molecular structures that emphasize specific modes. Methane specifically is a symmetrical polyatomic molecule descried as a spherical top[31]. Hydrocarbons, such as CH_4, have similar vibrational modes in the infrared region. While the strongest absorption lines for CH_4 occur in this midinfrared region, our sensor uses the near infrared region at 1651 nm (simulated spectra are shown in Figure 1.3). This is due to a variety of reasons that are described in more detail in a previous dissertation[25] by Laura McHale**.**

The equation shown below describes transmitted laser intensity, (due to absorption) known as Beer's Law.

$$T_\nu = \left(\frac{I}{I^0}\right)_\nu = e^{-k_\nu L} \tag{1.4}$$

Where T_ν is the fractional transmission, ν is the frequency, k_ν is the spectral absorption coefficient, and L is the absorption path length. Absorption can be found as $A_\nu = 1 - T_\nu$. The spectral absorbance is defined as $k_\nu L$ and will be further discussed in later sections. Furthermore, the absorption coefficient is

$$k_\nu = S\phi_\nu P_i \tag{1.5}$$

Where S is the line strength of the transition[31], ϕ_ν is the lineshape, and P_i is the partial pressure of the absorbing species. Rewriting 1.4 and writing the partial pressure as the pressure multiplied by the mole fraction, X_i, of the absorbing species gives:

$$T_\nu = \left(\frac{I}{I^0}\right)_\nu = e^{-S\phi_\nu PX_i L} \tag{1.6}$$

1.4.2 Resonant Cavity Theory

A second concept utilized by CRDS, resonant cavity theory, enhances the interaction time between light and matter. The sensor described in this thesis utilizes a linear two-mirror high-finesse cavity. The two-mirror cavity functions as a resonator for specific frequencies under proper alignment conditions. CRDS exploits the properties of high finesse optical cavities to gain sensitivity through increased interaction times between the light source and a species being detected.

Using Gaussian beam theory and ray transfer matrix analysis, one can analyze the properties needed to produce laser resonance within a cavity[32]. Gaussian beam theory is a very accurate approximation of plane wave propagation for the lowest transverse electromagnetic mode (TEM_{00}). In our case, the two-mirror resonator consists of two spherical mirrors both with a radius of curvature R. This configuration leads to the cavity having its own beam properties such as a waist and radius of curvature of propagation, which can be determined through ray transfer matrix analysis[33].

There are an infinite number of solutions to the wave equation corresponding to higher order TEM modes (e.g. TEM_{31}). Higher order modes are not desirable because of lower transverse spatial resolution[34] and reduced sensitivity.

In order to excite only the lowest TEM mode, the laser beam parameters must be carefully coupled to the cavity so that the beam and cavity have the same waist size and location. The radius of curvature of the mirrors is also matched to that of the curvature of propagation of

light. This is called mode matching[33]. The sensor used in this work accomplishes mode matching using an adjustable focus aspheric FC collimator (Thorlabs CFC-8X-C).

Within the cavity, electromagnetic fields become excited and increase intensity at specific frequencies[35]. Resonance within the cavity is produced by constructive interference. To constructively interfere effectively, it is necessary for the beam's phase to be the same after every round trip through the cavity. For this to occur, the round-trip phase must be integer multiples of 2π. From the solution of the derivation of the wave equation[35], one can find that if the mirror separation is d, the round-trip phase change, δ, is given by:

$$\delta = 2kd - 2(n + m + 1)\cos^{-1}(\pm\sqrt{g_1 g_2}) \tag{1.7}$$

Where n and m describe the TEM mode (n = 0 and m = 0 would describe the lowest Gaussian mode), and k is the wavenumber. g_1 and g_2 are $1 - \frac{d}{R_1}$ and $1 - \frac{d}{R_2}$ respectively, and R_1 and R_2 are the radius of curvature of the mirrors. In the case of CRDS where the two mirrors properties are matched, $R_1 = R_2 = R$ so that, $g_1 = g_2 = g$. From Equation 1.7, one can implement the resonance condition that occurs when the phase shift is an integral multiple of 2π. Then, one can solve for the resonant frequency.

$$\nu_r = \left(q + (n + m + 1)\frac{\cos^{-1}(\pm g)}{\pi}\right)\frac{c}{2d} \tag{1.8}$$

Where, c is the speed of light, d is the cavity length, and q is an integer. From this equation, one can see that the resonant frequency modes are spaced by the free spectral range, FSR, which also corresponds to the reciprocal of the cavity round-trip time[35].

$$FSR = \frac{c}{2d} \tag{1.9}$$

The finesse of an optical resonator (cavity) is defined as the FSR divided by the full width half maximum (bandwidth) at a resonant frequency. The finesse measures the spectral resolution of the cavity and a high finesse allows for an increased resonating of light within the cavity[36]. High finesse is achieved by using extremely high reflective mirrors of order R = 0.9999[36]. The finesse is calculated by dividing the FSR by the full width half max at a resonant frequency. The FWHM is:

$$\Delta\nu_c = 2\left(\frac{1-R}{\sqrt{R}}\right) \tag{1.10}$$

In this equation, R denotes the mirror reflectivity, not the radius of curvature. At the resonant condition where FSR = 2π, the finesse is then:

$$F = \left(\frac{FSR}{\Delta\nu_c}\right) = \pi\left(\frac{\sqrt{R}}{1-R}\right) \tag{1.11}$$

1.4.3 Cavity Ring-Down Spectroscopy

It is clear from Beer's Law that an increased path length over which the light interacts with the absorbing species can greatly increase the sensitivity for detection of a species. By coupling laser light into a resonant cavity, the light will reflect many times within the cavity thereby increasing the effective path length. To see how this works, one can first rewrite Beer's Law using the term which expresses the $\frac{1}{e}$ time of light decay known as the ring-down, $\tau(v)$.

$$T_\nu = \left(\frac{I}{I^0}\right)_\nu = e^{\frac{-t}{\tau(v)}} \tag{1.12}$$

Where T_ν is the fractional transmission, t is the time necessary for a cavity round trip, and $\tau(v)$ is the ring-down. The ring-down has a relation to the FWHM and the photon lifetime in the cavity shown below[36].

$$\tau(v) = \left(\frac{1}{2\pi\Delta v_c}\right) = \frac{L}{c}\left(\frac{\sqrt{R}}{1-R}\right) \tag{1.13}$$

When R~1, which is true in CRDS where R>0.999, the ring-down time for a cavity in vacuum, where the main source of loss is due to mirror reflectivity, can be approximated as the following:

$$\tau_o(v) = \frac{L}{c}\left(\frac{1}{1-R}\right) \tag{1.14}$$

L is the cavity length, c is the speed of light, and R is the mirror reflectivity.

When the species within the cavity provides additional loss due to absorption, the ring-down will decrease and can be expressed as:

$$\tau(v) = \frac{L}{c}\left(\frac{1}{(1-R)+k(v)l}\right) \tag{1.15}$$

Where $k(v)$ is the absorption coefficient of the species, v is the frequency, and l is the effective path length which increases due to resonance. Absorbance can be calculated by measuring the empty cavity ring-down, as well as the ring-down due to an absorbing species as:

$$A = k(v)l = \frac{L}{c\tau(v)} - \frac{L}{c\tau_o(v)} \tag{1.16}$$

Concentration of the given species can then be calculated through the following relation.

$$k(v) = S\phi_v PX_i \tag{1.17}$$

A common approach in CRDS is to scan the laser frequency across the absorption line and measure the frequency integrated spectrum rather than measuring at a single wavelength[37]. This requires knowing various line parameters which, in this work, have been simulated using HITRAN.

With an increase of path length of up to ten thousand times, CRDS increases its sensitivity by allowing much longer interaction times between light and matter. This increase in path length makes CRDS much more sensitive than direct absorption[31]. CRDS also has the advantage of measuring in the time domain which isolates the measurement from laser intensity fluctuations[34,37].

1.5 Thesis Objectives and Outline

The objective of this work is to continue the development, characterization, and improvement of a small open-path cavity ring-down spectrometer developed to measure trace amounts of atmospheric methane due to fugitive emissions from oil and gas facilities. The work presented in this thesis focuses on the following objectives:

1. Characterization and improvement of the sensor's accuracy, stability, and overall performance in varying conditions.
2. Verification of the sensor's detection capabilities during ground vehicle deployment field tests simulating real world oil and gas fugitive emissions.
3. Modification and deployment of the sensor on an unmanned aerial system (UAS) to test UAS detection and 3-dimensional plume mapping capabilities.

Chapter 2 discusses laboratory tests examining sensor stability and accuracy. It also discusses the development of a heater system which enables use of the sensor in low temperature conditions and the improvement of the sensors software fitting algorithm. Chapter 3 illustrates the results from a multitude of field-controlled release experiments which verify the sensor's ability to detect plumes in a simulated oil and gas emission scenario. The chapter also compares the sensor's performance in the field to a commercial analyzer in varying sensor configurations. Chapter 4 demonstrates the sensor's deployment on a fixed wing and rotor style unmanned aerial

vehicle. Controlled release measurements then also validate the ability to detect methane while mounted to UAV systems. In Chapter 5, conclusions of the work and possible future work for further improvements of the sensor are presented.

CHAPTER 2: Verification Tests

2.1 Closed-Path Measurements

Sensor accuracy was validated through a series of measurements performed within the lab using a temporary closed-path cell incorporated onto the open-path sensor. This closed-path cell allowed the delivery of fixed and known concentrations of methane. The closed-path cell was comprised of two seven-inch plastic tubes connected by a plastic tee. The cell was then mounted between the mirrors by using two more tees on either end of the cavity connected to "rain-blockers" on the sensor; these rain-blockers are normally used in the open-path configuration for mirror protection. The rain blockers have NPT threaded ends which allows for the mounting of the parts directly between the mirrors.

The center tee was used as the inlet to the closed-path cavity, while the two tees on either end of the cavity functioned as the release points. In its open-path configuration, the sensor employs a purge system which prevents dust and debris from contacting and dirtying the mirrors (Figure 1.2). The purge system flow works in reverse of the flow introduced into the closed-path configuration; therefore, it was removed and sealed to prevent unwanted ambient CH_4 from entering the cavity.

The gas delivery setup consisted of a gas cylinder mixture of ~250 ppm CH_4 and nitrogen balance coupled with another cylinder of ultra-high purity grade nitrogen. The tank of CH_4 utilized a mass flow controller (Celerity UFC-7360) calibrated for nitrogen. The amount of CH_4 within the tank in comparison to nitrogen was negligible when calculating flow rates. The ultra-high purity grade nitrogen tank incorporated an acrylic flowmeter (Omega FL-2040) with a range from 1-10 l/min. A direct ratio between concentration and flow rate was used to calculate the expected concentration within the cavity. A schematic of the setup can be seen in Figure 2.1.

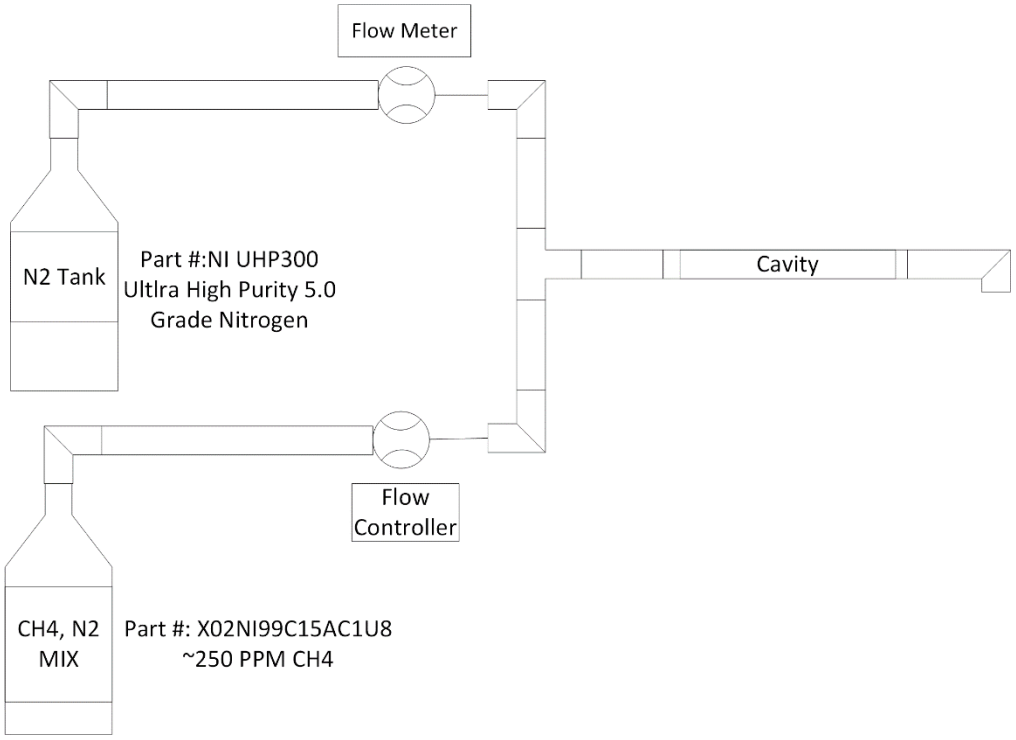

Figure 2.1: Schematic for gas delivery system used in closed-path validation measurements.

Figure 2.2 shows the results of the accuracy validation measurements for a series of expected concentrations. Each measurement consists of a sequence of two-minute averages of individual readings at one second intervals. The error bars on expected concentration are based on the uncertainties of the mass-flow controller and the rotameter, whereas the error bars on measured concentration were found as the standard error. Each measurement of concentration agrees with the expected concentration within experimental uncertainty.

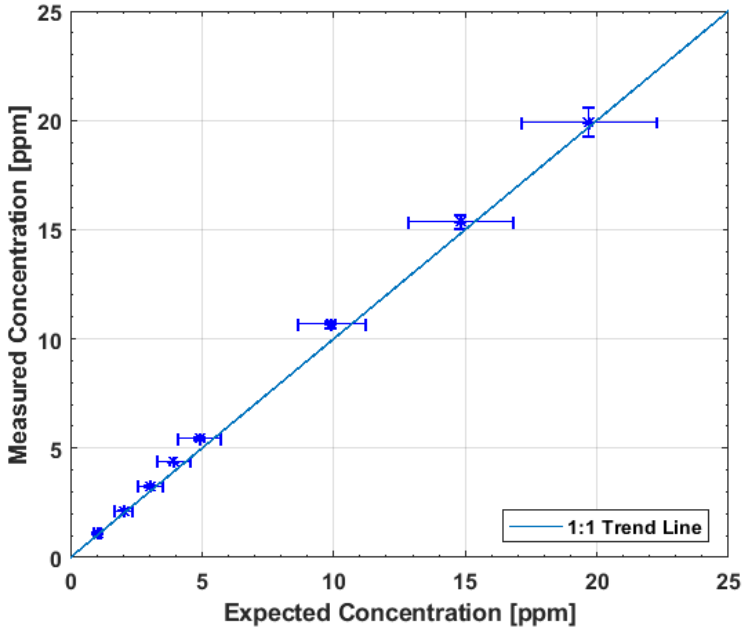

Figure 2.2: Plotted results of measured versus expected methane concentration which examines sensor accuracy.

To have more accurate knowledge of the expected concentration within the cavity, another verification was done by using a gas cylinder with a mixture of four ppm CH_4 and nitrogen balance. The setup in this case only utilized one tank of gas, as diluting with nitrogen was not needed. Figure 2.3 below shows the setup for the ~4 ppm validation test.

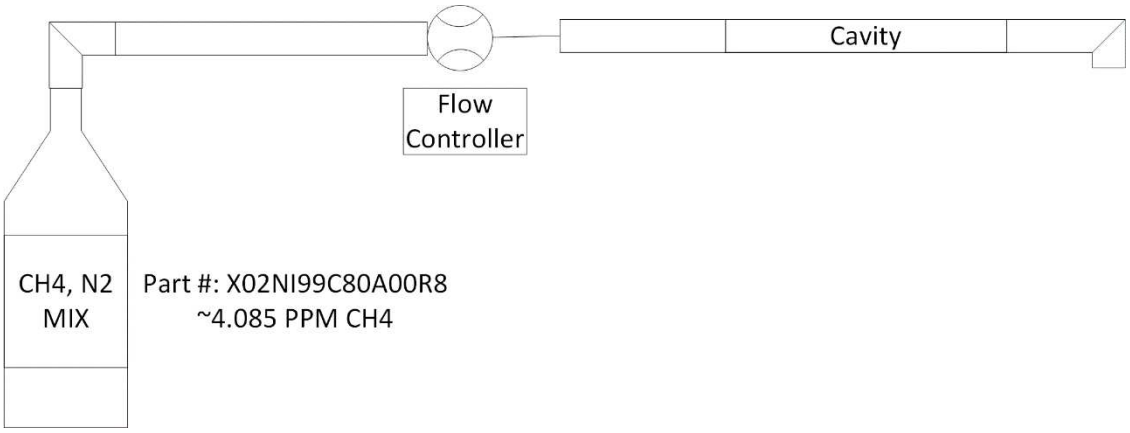

Figure 2.3: Schematic for gas delivery system modified for single CH_4 cylinder.

Through this test, an average concentration of 4.115 ± 0.022 ppm was measured. The precise concentration of the tank was 4.085 ± 0.204 ppm. This close agreement further shows the sensor's ability to detect trace concentrations of methane accurately.

Precision of the sensor was calculated through Allan variance analysis[38,39]. Allan variance is a common statistical method used to measure frequency stability developed for atomic clocks. This work employs a modified Allan variance used for continuous wave cavity ringdown spectroscopy[39]. Results for the Allan variance analysis on the open-path sensor in laboratory conditions are shown below in Figure 2.4. In stable laboratory conditions, the open-path sensor has an Allan deviation (square root of the Allan variance) range of 10 ppb – 15 ppb for 1 second averaging time. The range depends on air cleanliness in the lab (due to Mie scattering) and sensor alignment conditions.

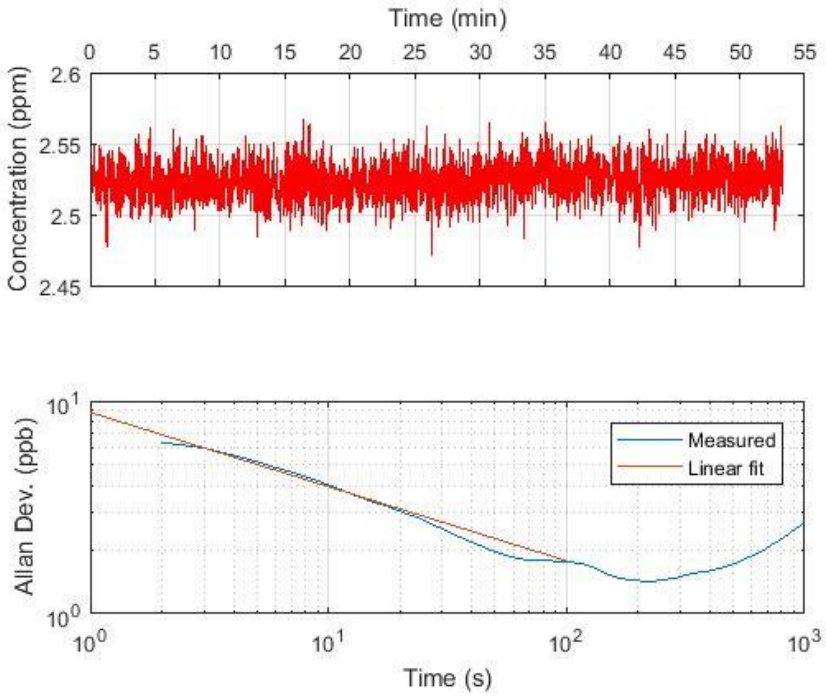

Figure 2.4: Top: Measurement of CH_4 concentration data. Bottom: Allan Deviation plotted against sample time.

2.2 Comparison Against Reference Analyzer

Lastly, to offset any possible error in the expected concentration, validation measurements were performed against a commercial closed-path CRDS instrument (G2203 Picarro Analyzer). A small modification was made to the gas delivery system for these tests. Figure 2.5 illustrates the modification of incorporating a line from the sensor cavity output to the Picarro inlet. Since the Picarro inlet has a flow rate of (0.1 – 0.5 l/min), a tee was placed before the inlet to assure that the Picarro would not over pressurize[40].

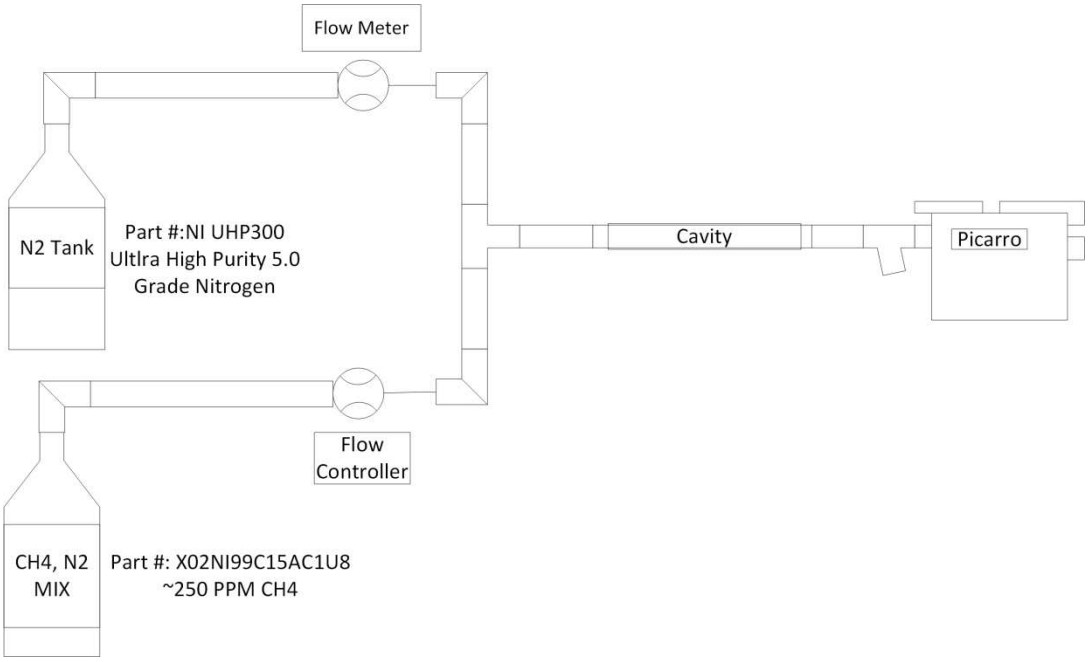

Figure 2.5: Schematic for gas delivery system modified for use with G2203 Picarro Analyzer.

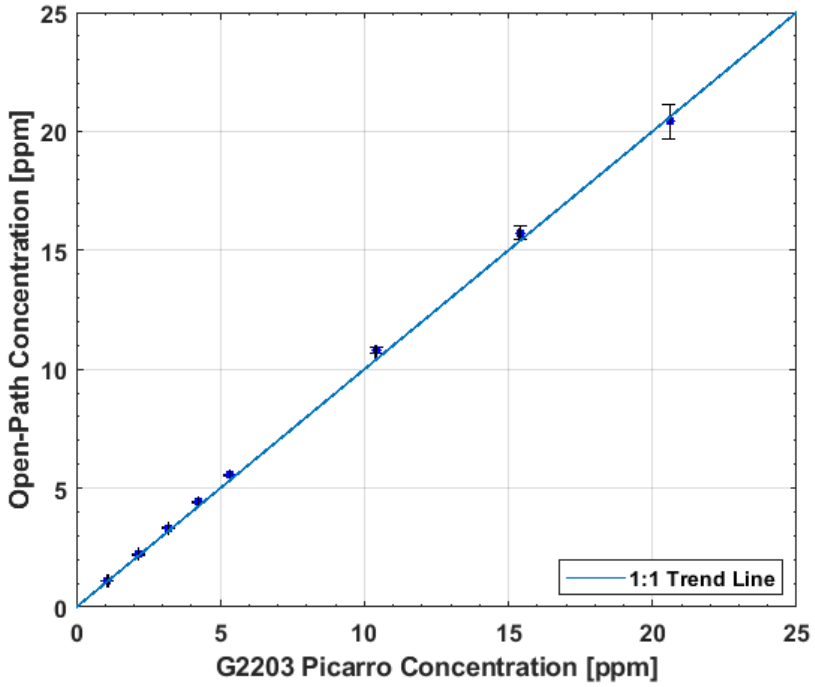

Figure 2.6: Results of measured versus expected methane concentration for CSU sensor and G2203 Picarro.

In this case, each measurement was made from an average of eight-minute individual readings from each sensor. Larger averaging times were taken in this test to attempt and reduce fluctuations in readings. The error bars were calculated as the standard error of each sensor. Again, one can see from the results in Figure 2.6 that the open-path sensor performed very well in comparison to the Picarro. These results are important in validating the open-paths performance compared to the Picarro closed-path configuration. The close agreement between methods displays the open-path's ability to be as accurate as closed-path sensors but without the need to use as much power and effort on controlling all the parameters within a vacuum cavity (e.g. pressure and temperature to reduce broadening). The open-path sensor's measurements again lie well within the error margins of expected concentration and overlap in close agreement with that of the Picarro.

2.3 Environmental Exposure Tests

2.3.1 Heater Design and Testing

Phase III of the sensor was designed using carbon-fiber with a very low coefficient of thermal expansion (CTE) due to the sensitivity of CRDS to thermal effects. Because of the extremely precise (High-Finesse) optical cavity, micron sized deformations can cause sensor alignment degradation. The degradation to cavity alignment caused by thermal deformation requires a heater system to prevent these effects at low temperature. A heater system was thus designed and implemented on sensor heads to prevent loss of signal in low temperature conditions.

The design is simple yet effective in producing enough heat to prevent misalignment while also keeping the power consumption increase of the sensor minimal (<40 W). Each heater consists of a high density Comstat cartridge heater (MCH2-80W-001), an Orion fan (OD4010-12LB), and a heat sink (Advanced Thermal Solutions Inc. ATS-54400D-C1-R0). The high-density cartridge heaters were inserted diagonally into the heat sinks. The fans were then mounted in opposing directions to encourage circulation of the air in each cap. Custom 3-D printed mounts were designed to hold two heaters within each sensor head. A custom tube heater for the tube connecting the two heads was also designed and tested, however, its role was deemed negligible in comparison to the other heaters.

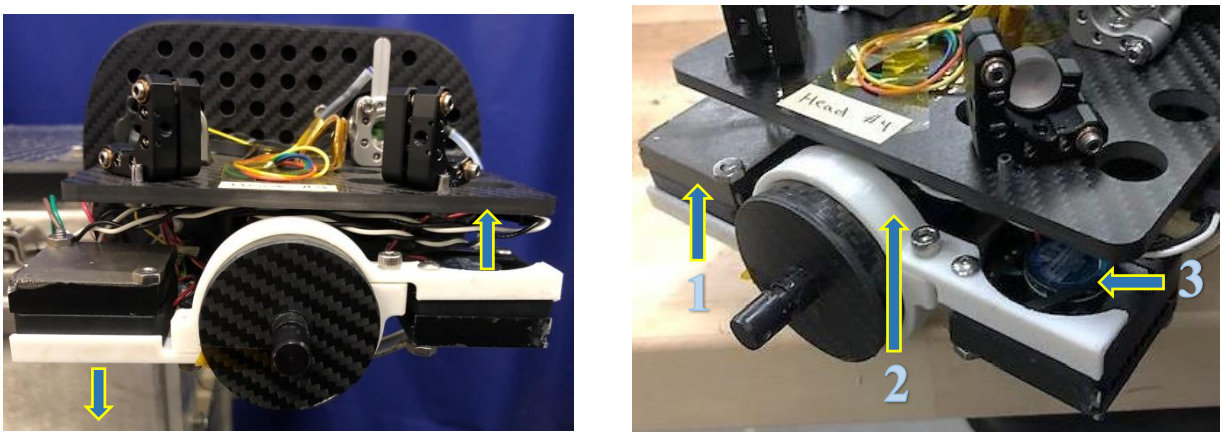

Figure 2.7: Photographs of layout of the heating system. Left: Arrows indicate the fan flow direction. Right: 1: Heater/heat sink unit. 2: 3-D printed mount. 3: Fan.

The internal temperature within each of the sensor bulkheads was controlled to 25°C. Resistance temperature detector (RTD) probes coupled with PID controllers (Meerstetter TEC-1091) were used to monitor and control the temperature**.** To fully integrate the sensor for low temperature conditions, exterior insulation was wrapped around the bulkheads and the tubing between them. Tests were conducted outside, as well as in cold chambers capable of reaching -30°C. Figure 2.8 shows an example of sensor performance for outside operation at ~2^{o}C.

Two main parameters were examined when deducing the effectiveness of the heating system. The first parameter was accurate background concentration reading, which is generally in the range of 2.0 ppm in Fort Collins. The second parameter was ingestion rate. Ingestion rate is the amount of ring-downs (τ) the sensor produces per second for fixed laser scan conditions. It is directly related to how well the laser cavity is aligned. The higher the ingestion rate, the more resonant peaks are being detected at a given photodiode detector voltage level; therefore, the cavity is better aligned. Generally, the ingestion rate goal is 500 τ/s, but anywhere above 300 τ/s is considered suitable. One can see that as the heater system reaches its set point both ingestion

rate and concentration stabilize at appropriate levels for field use quality control (QC) metrics (e.g. ingestion rate would be used to admit/reject the concentration data).

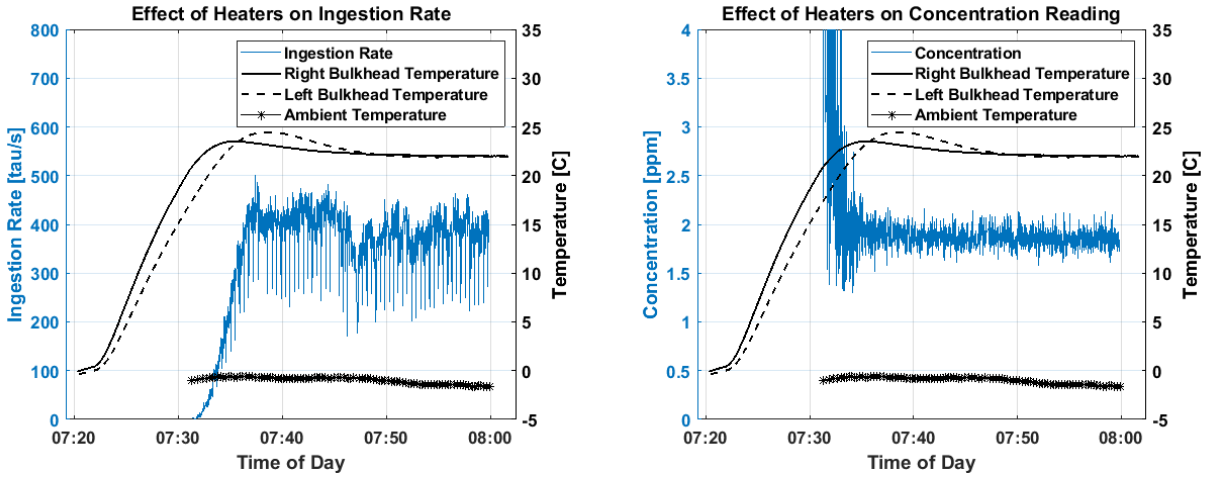

Figure 2.8: Left: Temperature of the two sensor bulkheads, ambient temperature, and ingestion rate against time. Right: Similar plot with concentration rather than ingestion rate.

2.3.2 Long-Term Exposure Test

One main goal of this work is to produce a sensor that has long-term performance stability. To test the ability of the sensor to stay aligned over long periods of time in harsh, uncontrolled conditions, a long-term weather exposure test was conducted over four months (February – May 2019). The test involved leaving sensor outdoors with minimal supervision. Only monitoring the data occasionally, the test was implemented to infer how long the sensors could continue taking reasonable data without the need for realignment in stationary deployment.

Ingestion rate, baseline level, and concentration data were examined to infer sensor performance. The three parameters (at fixed trigger level) demonstrate the performance of the sensor by monitoring mirror reflectivity (baseline, b in equation 1.2), alignment precision (ingestion rate), and fit stability (concentration). The reflectivity of the mirrors can degrade due to lack of cleanliness (e.g. dust or moisture depositing on mirror surface) while alignment

precision denotes how well the laser is mode matched to the cavity. Data were analyzed on multiple days throughout the experiment. Table 2.1 below shows the data collected on a few days over the span of the test. The data on day one was collected inside the lab before placing it outside to produce a baseline alignment level. Due to thermal effects on the cavity, a decrease in ingestion rate can be seen at lower temperatures (though remaining above 300 τ/s), while the baseline (mirror reflectivity) remains constant. The sensor was successfully able to produce accurate readings for a total of 76 days without realignment before a loss of signal occurred. These results confirm the ability of the heaters to produce good data even in winter conditions. Through this trial, the sensor demonstrates its robust design and dependability over a long-term stationary deployment.

Table 2.1: Ingestion rate, baseline, concentration, and temperature values of data taken by sensor over the full span of the long-term exposure test.

	Ingestion Rate [tau/s]	**Baseline [cm^{-1}]**	**Concentration [ppm]**	**Temperature [C]**
Day 1 (Lab)	614 ± 121	$(8.96 \pm 0.39)10^{-7}$	2.69 ± 0.03	22
Day 3	371 ± 33	$(1.03 \pm 0.024)10^{-6}$	2.09 ± 0.05	2
Day 14	465 ± 43	$(1.03 \pm 0.031)10^{-6}$	2.03 ± 0.07	10
Day 29	449 ± 40	$(1.04 \pm 0.020)10^{-6}$	2.00 ± 0.04	13
Day 51	687 ± 121	$(1.02 \pm 0.039)10^{-6}$	2.06 ± 0.05	23
Day 76	438 ± 40	$(1.04 \pm 0.018)10^{-6}$	1.89 ± 0.04	12

2.4 Modifications to Spectral Fitting Algorithm

2.4.1 Modified Single-Peak Lorentzian Fit

Several data acquisition and fitting issues were apparent in previous iterations of the sensor software. These issues caused periodic loss of data (“dropouts”) and added noise in the concentration measurements. Modifications were made to the LabVIEW fitting algorithm to

address these issues. The fitting algorithm and the modifications implemented in Phase IV are explained below.

The fitting method described in section 1.3.2 proved to be accurate but is inherently computationally expensive. This expense, coupled with other factors, led to the production of random "dropouts" in the data where the algorithm would fail to iterate and give the initial guess parameters as the solution to the fit. To help reduce the volume of "dropouts" produced, a modified single-peak Lorentzian equation with comparable accuracy but less computational cost was implemented.

As seen in Figure 1.3, the summation of the four absorption lines creates a single feature. While the peak is not an exact Lorentzian, it was found that modeling it as such was effective in producing accurate readings. The new fitting equation uses one Lorentzian equation to fit the single-peak rather than summing four individual Lorentzian curves. In order to keep the accuracy in concentration readings, the new fitting equation must also be robust over similar temperature and pressure spans.

From Equation 1.2, the single-peak in Figure 1.3 can be modeled. By modeling the single-peak as a Lorentzian curve, the resultant equation is:

$$k(\nu) = b + \left(\frac{1}{\pi}\right)\frac{P^2}{T}[CH_4]\frac{S * C}{(\nu - \nu_0 + \nu_s)^2 + (P * C)^2} \tag{2.1}$$

For this single effective absorption line, it is necessary to determine the appropriate values of line strength, S, peak center, ν_0, and pressure broadening coefficient**,** C. The line strength was calculated by directly summing the four contributing line strengths to derive a new temperature dependent equation. Minimization was then used to modify the line strength to produce more accurate live measurements. The solutions for the parameters were compared to

simulated and measured data to deduce the parameters with the most accuracy over a range of likely conditions the sensor would encounter. Figure 2.9 demonstrates the new fitting algorithm's ability to recover the four-peak simulated CH_4 accurately over a wide range of temperature and pressure.

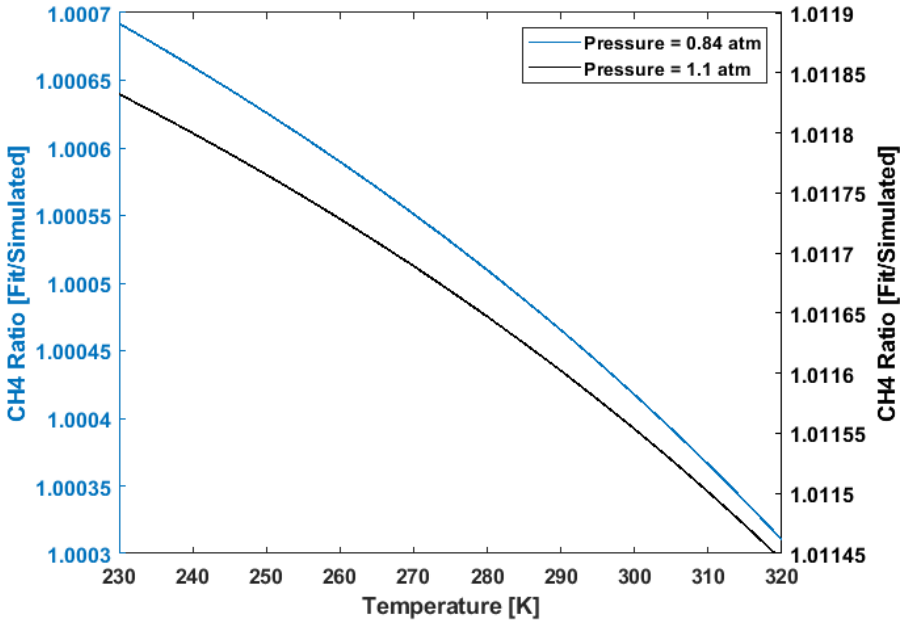

Figure 2.9: Ratio of fitted CH_4 to initial simulated CH_4 over a range of temperatures at two different pressures based on spectral simulation.

The new fitting algorithm was also verified using data collected in the laboratory to ensure agreement between the previous four-peak fit and the new single-peak fit. Using the set up seen in Figure 2.3, a known concentration of methane was introduced into the cavity. A difference of less than 0.15% was measured between the two fitting methods, which is well within the tank concentration uncertainty and experimental uncertainty. The use of the new single fit method greatly reduced the overall dropout percentage (from ~10.5% to ~4%) as can be seen in Figure 2.10. The new method brings computational advantage while not reducing the accuracy of the data.

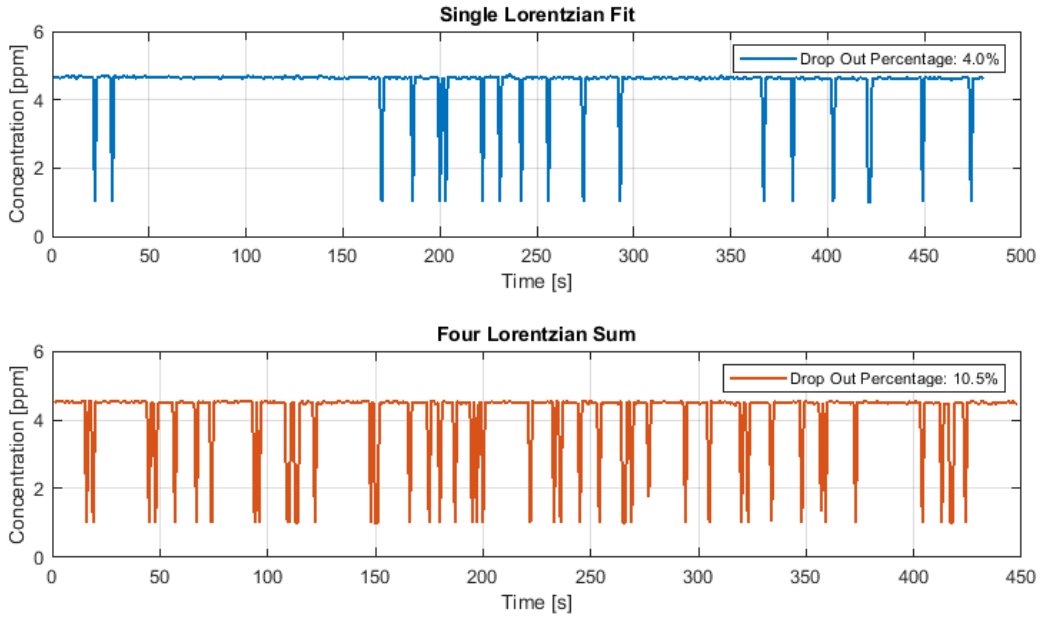

Figure 2.10: Time series of CH_4 concentration for single/four-peak fit: top/bottom. Note the reduction in "dropouts" for the single-peak fit.

Additional work in this regard has been done with the help from a CSU undergraduate student, Anthony James Puga, to further reduce the number of dropouts produced by the fitting algorithm. A new algorithm written by Puga in MATLAB utilizing data binning was implemented into the LabVIEW software through Mathscript. Using a single Lorenztian approximation coupled with the new Mathscript method successfully reduced the dropout percentage to below 0.1%.

CHAPTER 3: Ground Based Field Tests

The overall goal of this sensor is to be easily field deployable and accurately map methane plumes from emission sources due to oil and gas facilities. There are three facets that work of this nature is interested in: the detection, localization, and quantification of emissions[23]. Localization and quantification require plume dispersion modeling using wind velocity measurements. The work presented in this thesis focuses on the leak detection capabilities of the sensor, but other work with collaborators is also being done to examine localization and quantification[26].

Characterization of the sensor's detection of methane emissions (analogous to that of oil and gas facilities) were done by simulated release experiments. Experiments test detection limits through varying distances, emission rates, and wind conditions. The sensitivity of the sensor baseline in these varying ambient conditions was also examined using Allan variance analysis. The sensor's ability to function continuously in a mobile, uncontrolled setting was also crucial during these tests. The system was constructed to be relatively mobile due to wind direction uncertainty, and for the ease of set up. Observations of controlled release experiments were then gathered.

3.1 Controlled Release Experiments

Controlled release experiments with known mass flows were used to simulate point-source methane emissions. Experiments were done at Christman Airfield located in Fort Collins, Colorado, over the course of several months. Twenty-two total releases were conducted. A cylinder of chemically pure (99.5%) CH_4 delivered with a mass flow controller (Sierra SmartTrak 50) were used as the emission source. Emission rates ranged from 0.1 g[CH_4]/s to 0.5 g[CH_4]/s (~9 - 45 l/min).

A weather station (Campbell Scientific, CR1000 and NL115) with ultrasonic anemometer (Campbell Scientific, CSAT3) was used to simultaneously record and acquire time series data of wind velocity amplitude (20 Hz rate). Plumes were captured at varying distances up to 500 meters from the source. Vehicle paths around the emission point were adjusted depending on wind magnitude and direction. The components for the controlled release setup are shown in Figure 3.1.

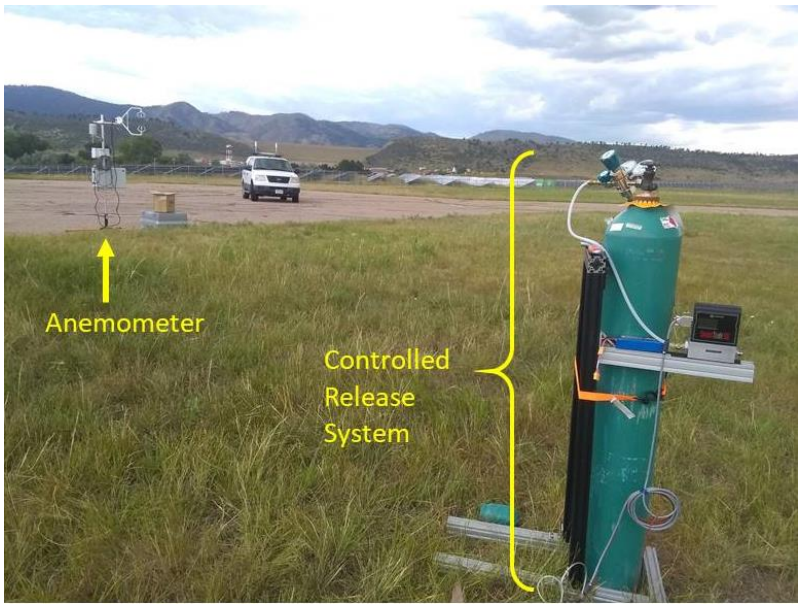

Figure 3.1: Photograph of the setup used in producing a controlled release experiment at Christman Airfield.

The sensor was mounted on the roof of a Ford Expedition using a standard roof-rack. A custom aluminum mount was designed to reduce vibrations while driving. The sensor can run directly off of the vehicle battery (12-18 volts), but because of its low power draw, it was run off a 2000 mAh LiPo battery for ease of removal. The sensor was taken off the vehicle after every test to check its alignment and to do further testing in the lab. Temporal and spatial localization data were taken using a GPS sensor (Linx, RXM-GPS-FM-T). Data was collected and fitted at

one second measurement intervals in real-time. The sensor mounted on the Ford Expedition can be seen in Figure 3.2.

Figure 3.2: Phhotograph of sensor mounted on Ford Expedition.

3.1.1 Sensor Performance

Sensor alignment was monitored throughout the controlled release tests. Field tests on previous sensor iterations had misalignment issues after only a few hours of testing[25]. Modifications made to the sensor (Phase IV design), such as new rain blockers and a heating system, allowed the sensor to better keep its alignment throughout the current testing.

Over the 25 days of field testing, alignment was kept for a majority of the time. Only a few minor realignments were needed to keep sensor performance at its peak condition, though these realignments were not crucial to the continued use of the sensor. Furthermore, realignment in the field, which has been common in the past, was never needed. The ability to keep alignment

and stable data confirms improvements of Phase IV over previous phases. These tests further prove the robust opto-mechanical structure of the sensor. The sensor's insensitivity to vibrations and its capability of operating on a moving vehicle is also demonstrated.

Stability and precision were monitored by Allan variance analysis. The Allan deviation of the baseline for every controlled release test was calculated. The detection of plumes above background concentration depends on the sensor's sensitivity. Elevated plume readings were removed from the baseline when calculating deviation to prevent bias. This was done by using a robust program in MATLAB that locates all local maximums that are greater than the upper 95% confidence interval of the mean for all the data. Those points are then removed and a new mean and moving average are calculated. Figure 3.3 shows example data for controlled release test done on April 25th, 2019.

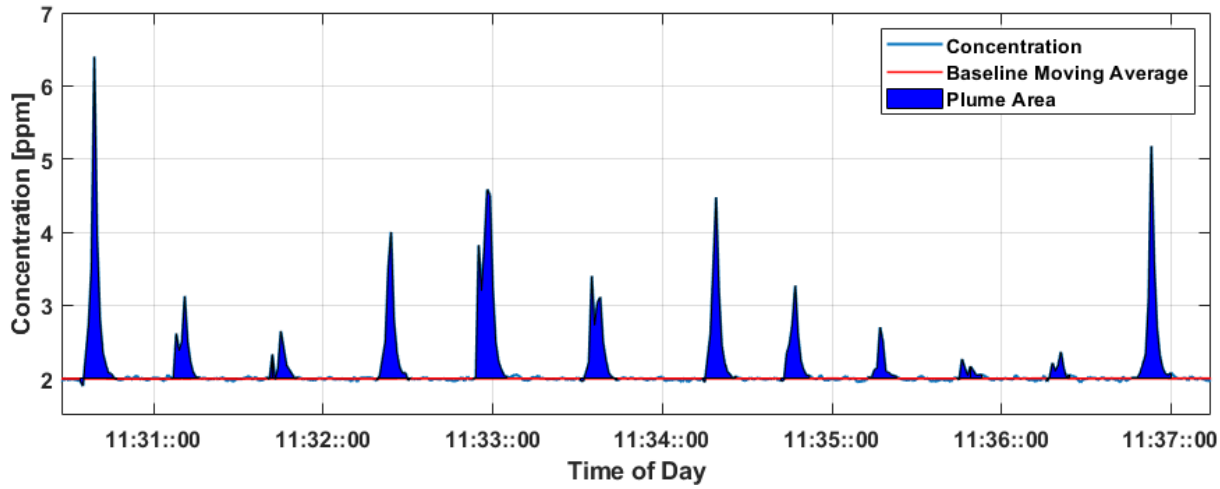

Figure 3.3: Plume data plotted against time.

Once the plume outliers were removed, the baseline Allan deviation was calculated. Over the entire 22 field tests, the sensor's average Allan deviation was ~43 ppb. The Allan deviation reduces to ~35 ppb when rejecting segments with a lower than ideal trigger level. Low trigger levels could be due to detector influence from ambient sunlight. Degradation of sensitivity in the

field compared to that within the lab (by a factor of ~3) is attributed to several factors. One factor is particle loading in the air that periodically produces noisy data (Mie scattering). Noisy data due to Mie scattering was more apparent during the commute from the laboratory building to the test field where exhaust from cars caused a notable effect. As mentioned in previous work[25,27], sensor sensitivity also has a dependence on temperature. While the heaters help prevent this increase in noise in cooler temperatures, warmer temperatures also produce a similar thermal degradation which was apparent on warmer summer days during testing. For tests where the average temperature was ~21°C the Allan deviation of the baseline was 21 ppb. To contrast, when the average temperature was 35°C, the deviation was 60 ppb (though the sensor can be aligned at higher temp to counter high temperature effects).

3.1.2 Detection

Plume detection was examined over a range of emission rates. Over 2000 individual plumes were sampled over the course of this study. An example of the detected plumes can be seen in Figure 3.3. The detection limit for methane mass flow (as opposed to concentration) depends on distance to the source and wind conditions. For the conducted tests, with relatively consistent winds on the average of ~3 m/s, the observed (peak) plume concentration showed a close agreement with Gaussian dispersion models as seen in Figure 3.4.

The dispersion equation[41,42] used to model the plume is:

$$C(x,y,z:H) = \left(\frac{Q}{2\pi\sigma_y\sigma_z u}\right) e^{\left[-\frac{1}{2}\left(\frac{y}{\sigma_y}\right)^2\right]\left\{\left[-\frac{1}{2}\left(\frac{z-H}{\sigma_z}\right)^2\right]+\left[-\frac{1}{2}\left(\frac{z+H}{\sigma_z}\right)^2\right]\right\}} \quad (3.1)$$

Where Q is the emission rate, u is the wind speed, x, y, and z denote the position where $x = 0$, $y = 0$, and $z = 0$ would denote the emission point source location at ground level. H is the stack height, and C is the concentration. σ_y and σ_z are the standard deviation in the crosswind and

vertical direction of the plume concentration distribution. σ_y and σ_z have been found to be functions of downwind position (x), and atmospheric stability conditions. Pasquill-Gifford curves give values for σ_y and σ_z for given distances downwind and stability class (Figure A.2 and Figure A.3). σ_y and σ_z were computed through the use of empirical equations which approximately fit Pasquill-Gifford curves as a function of distance (x) away from the source[43]. The stability class was chosen by averaging the wind data to narrow the stability range as seen in Figure A.1. Of the three stability classes in that range, the one which produced the best fit (stability class C) was chosen. To retrieve the curve of concentration as a function of distance from the emissions source at the height of the vehicle (where the sensor is mounted), y = 0 m, z = 2 m, and H = 1 m. The concentration scales linearly with emission rate. The data shown incorporated an emission rate of ~45 l/min (~0.5 g/s). For this mass flow, the sensor was able to detect a plume up to 320 meters away.

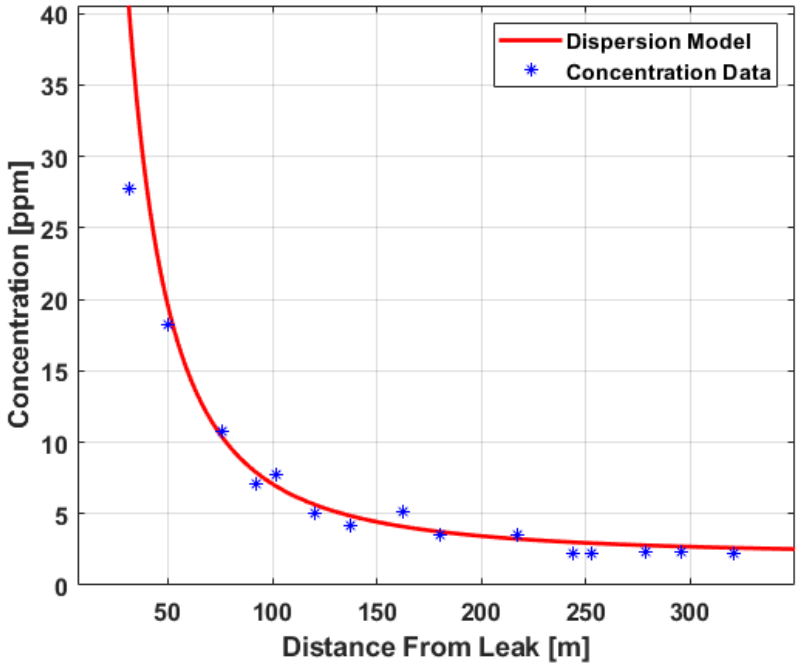

Figure 3.4: Plot showing Gaussian dispersion curve along with sensor concentration data as a function of distance from emission source.

Figure 3.5 shows a bird's-eye view of the detection of elevated plumes for tests done on June 6th, 2019. Elevated plumes were measured 70 meters away from the emissions point on this specific day. The plot also shows wind direction and magnitude and its variability over the full range of the test. The data clearly shows the capabilities of the sensor to detect trace gas leaks downwind at a variety of emission rates and distances. In previous tests, plumes were detected for mass flows as low as 6 l/min.

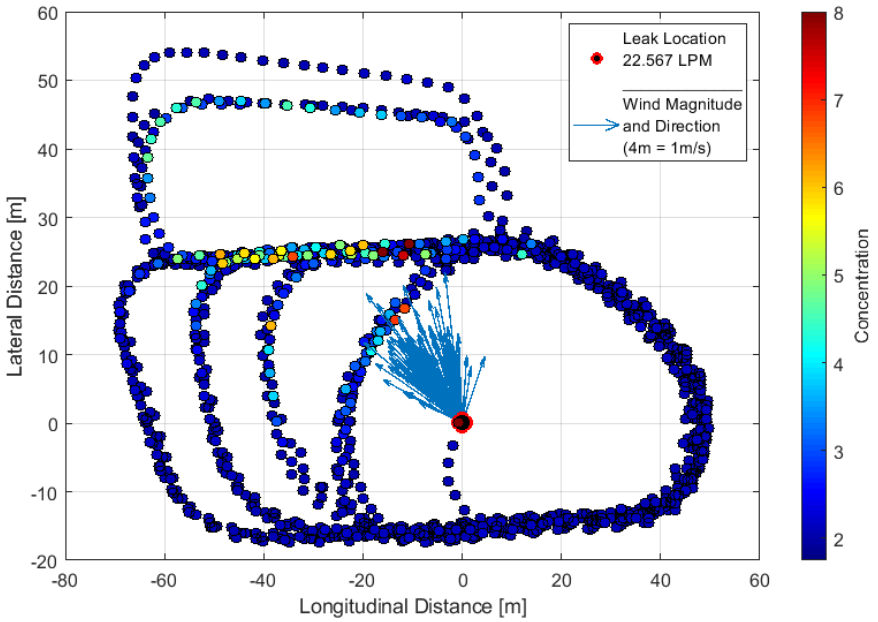

Figure 3.5: Full aerial view of controlled release test on June 6th. A variety of paths were taken to accurately map the plume dispersion downwind of the leak location.

Plume measurements can vary substantially with given mass-flow, distance, 2-dimensional plume shape and various other parameters. Because of this, distance integrated plume area measurements are useful when quantifying emissions because they consider total methane across the plume rather than only the peak concentration value. The plume area contour is plotted in Figure 3.3. The area of each plume is integrated over the drive length and the

baseline is subtracted to get the total path measurement in units of ppm*m. This is particularly helpful when comparing varying detecting methods e.g. open-path, Picarro, UAV mounted where, for example, different sensors may have different time responses. Work done by Laura McHale[25] studied the effects that 1 Hz vs 3 Hz sampling times had on plume areas. Her findings demonstrated that 1 Hz sampling time slightly underestimated plume area. This finding is further investigated in later sections of this thesis.

3.1.3 Comparison Against Reference Analyzer

As with lab measurements, to validate the open-path sensor's ability to detect plumes, a Picarro was used as a reference. The same G2203 Picarro analyzer mentioned in Chapter 2 was used for these measurements. The open-path sensor was mounted on a vehicle which was modified to carry the suite of components needed for the Picarro analyzer (e.g. vacuum pump, computer monitor, high power source). The inlet of the Picarro was located as close to the open-path cavity as possible. The response time of the Picarro is rated at < 3s but varies with the length of tubing. As was expected, the Picarro analyzer exhibited a noticeable 5-9 second lag in detection time as seen in Figure 3.6. Lag time caused by flow cells can distort mobile data and complicate the process of localization[44,45] (note that even for a given sensor the exact lag time can vary with pump setup and filter health).

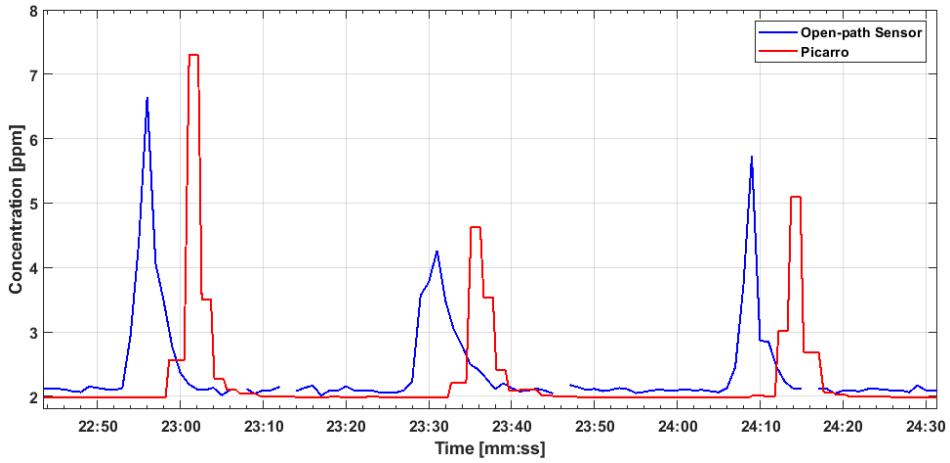

Figure 3.6: Overlay of Picarro and Open-Path sensor data for the same time span.

A comparison of peak concentration and integrated plume area values between the two methods was also done. For concentration values below ~10 ppm the open-path sensor showed close agreement with the Picarro analyzer. For values above ~10 ppm, the open-path sensor displays regular underestimation of plume size (peak and area). As can be expected, underestimation of plumes was much more prevalent at higher emission rates due to higher overall methane concentration at equal distances.

These findings are consistent with findings mentioned in McHale's dissertation[25]. One of the main issues that causes this effect stems from the aerosol software filter's rejection of data when methane concentration changes rapidly (<1 second). While one of the contributing factors to this issue discussed in the previous dissertation is the difference between 1 Hz vs 3 Hz sampling rates, the data within this thesis was processed in real-time rather than post processed. Real-time processing of the data is vital to quick analytical turn around which is needed in real world scenarios. Post processing ample amounts of data takes too much time and requires much larger storage memory which Phase IV is trying to move away from. Due to this, other more suitable solutions are being developed.

Another cause for the underestimation of the plume sizes is believed to be the standard fitting algorithm used in the LabVIEW software. Therefore, more work is currently being done in this regard to attempt and resolve this issue without changing the sampling rate. The binning algorithm described in section 2.4.1 is one such solution. Recent preliminary laboratory tests as well as field tests show promise in the new binning method's ability to measure much higher concentration values. With the old LabVIEW fitting method, max concentration measurements for a leak rate of ~45 l/min (~0.5 g/s) were at ~ 40 ppm**.** The new method was able to measure up to 90 ppm in the field. Measurements of this magnitude were previously not possible in lab experiments.

Figure 3.7 and Figure 3.8 demonstrate a 1:1 comparisons of data collected by the open-path sensor and the Picarro analyzer for two flow rates. It is important to note that peak plume values vary significantly over tests due to the complexity of plume dispersion as well as changing wind and driving patterns. Data for a leak rate of ~22.6 l/min (~0.25 g/s) exhibited very good agreement of plume size between the two detection methods. A difference of only 4% and 2% between a fitted line and a 1:1 trend line was seen for peak concentration and plume area measurements respectively.

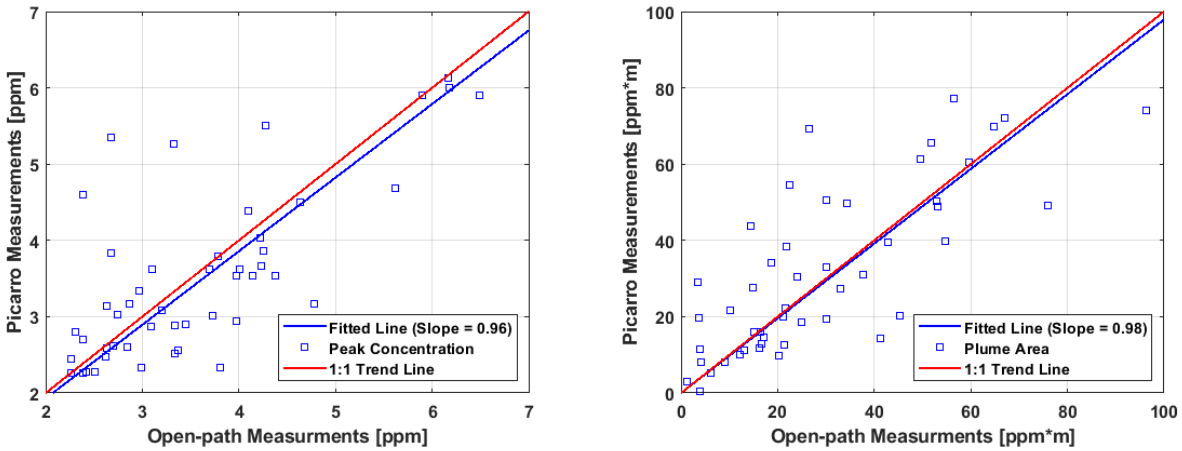

Figure 3.7: Left: 1:1 comparison and fit of methane peak concentration for Open-path and Picarro. Right: 1:1 comparison and fit of integrated plume area of Open-path and Picarro. All measurements were taken at ~0.25 g/s.

Data for a leak rate of ~0.5 g/s exhibited underestimation of plume size due to fitting errors ("dropouts" within plume reading or concentration values higher than ~12 ppm) and therefore were removed from the plot. Data for this higher leak rate showed a 13% and 16% difference between the fitted line and a 1:1 trend line. Underestimation of plume size was less prevalent at lower leak rates due to lower overall concentrations. Common fitting errors which produce underestimation of peak concentration have been greatly reduced since the acquisition of this data through the development of better fitting algorithms (binning fit), but more data has yet to be collected with the Picarro due to unavailability.

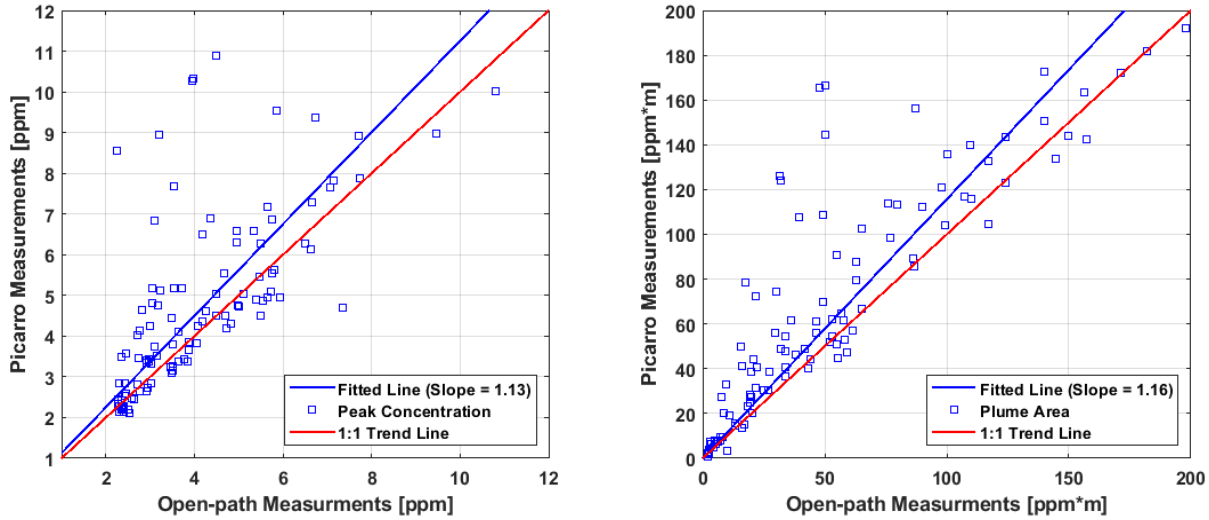

Figure 3.8: Left: 1:1 comparison and fit of methane peak concentration for Open-path and Picarro. Right: 1:1 comparison and fit of integrated plume area of Open-path and Picarro. All measurements were taken at ~0.5 g/s.

3.1.4 Testing of Perforated Tube (Particle Filter) Along Beam Path

A common issue that arises with the use of open-path designs is the exposure of the high reflectivity cavity mirrors to ambient conditions. While the free flow of ambient air into the cavity allows for fast response times and simplified hardware systems, it also allows particles (e.g. dust, water droplets, etc.) within the cavity leading to two issues. First, particles on the order of or larger in magnitude of the wavelength of the light cause optical extinction by means of Mie scattering. This scattering degrades the signal by producing noise in the spectrum[25]. Methods used on this sensor for mitigating this effect include an aerosol software filter described further in the next section. Second, dust particles can degrade the reflectivity of the mirrors by depositing directly on them. The resonant cavity relies on the reflectivity of the mirrors staying above ~99.99%. Dust or debris can degrade the reflectivity as has been encountered when dealing with mud, rain, and snow during long term deployment operations.

To attempt to curb the possibility of debris causing degradation or loss of signal, the sensor employs a purge system which restricts large particles from making contact with the mirrors (see Figure 1.2). The purge system utilizes a small low power pump which pushes filtered air towards the high reflectivity mirrors and outward in the direction of the cavity. While generally successful, the purge system has shown to be inadequate at times when vehicle speeds are high and conditions are poor (e.g. rain). The longevity of the sensor requires that the mirrors stay clean for as long as possible under very harsh conditions. Therefore, more work to mitigate this effect has been done.

A mechanical perforated particle filter was designed and implemented onto the open-path cavity to test its viability for reducing signal degradation caused by large particles. The perforated filter's effect on methane detection was analyzed to assure overall performance remained intact. Various parameters were analyzed comparing the consistency of two hardware approaches under the same conditions. The perforated filter consists of two cylindrical perforated metal tubes and is mounted over the cavity through the use of two 3-D printed brackets**.** An image of the perforated filter and its mounting method over the cavity can be seen in Figure 3.9**.** Similar filtering structures have been used in other work investigating open-path sensor designs[23,46].

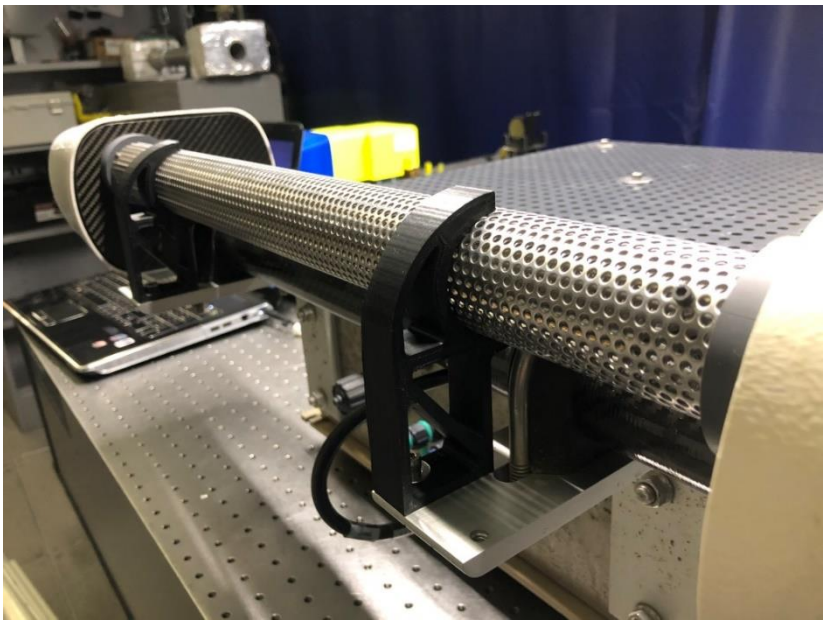

Figure 3.9: Photograph of mechanical perforated tube mounted onto the cavity. The 3-D printed mounting brackets can be seen in black.

The filter was used throughout controlled release testing and was installed and uninstalled as testing required. Tests were conducted consecutively. The perforated filter would be used for one test and removed for the next. Quick turnaround during consecutive tests allowed for decreased variability in day to day wind patterns as well as drive path differences. Averages of the concentration baseline and of the Allan deviation of the baseline were recorded for each trial. Ingestion, trigger, baseline, drop out percentage, and tau preserved percentage were also monitored. Tau preserved percentage analyzes the amount of data points which are removed from each fit due to aerosols. Under very noisy conditions where there is substantial particle loading in the air, the tau preserved percentage will drop. “Dropout” percentage expresses the amount of fits that are unsuccessful due to the fitting algorithm as described in section 2.4.1 and in Figure 2.10. Over all of the examined parameters, the perforated filter configuration showed no significant change in the data shown in Table 3.1. This lends to the viability of using the filter in long term continuous deployments without it degrading the data.

Table 3.1: Data demonstrating the effects of the mechanical perforated filter on performance parameters of the sensor.

	Allan Deviation [ppb]	Average Baseline Concentration [ppm]	Average Ingestion [τ/s]	Average Trigger [V]	Average Baseline [cm^{-1}]	Drop Out Percentage	Tau Preserved Percentage
No Filter	44.20	2.04±0.05	490±107	0.21±0.02	1.04±0.05	6.03	97
Filter	40.41	2.06±0.04	488±86	0.21±0.02	1.02±0.05	6.31	98

The plume detection ability of the sensor with and without the use of the perforated filter was also investigated. The main concern with the mechanical filter's use, is the possible perturbation of the free flow of air which enters the cavity. Average peak plume concentration measurements and integrated plume area measurements for each trial (with and without the particle filter) during controlled releases were monitored. Figure 1.1 displays these averages over two plots. Data over 19 trials (38 individual runs) using the perforated filter showed no significant change with respect to data collected without using a perforated filter. All data points overlap to at least one standard deviation. The mean and standard deviation overall for plumes measured with the use of the particle filter and without the use of the particle filter are 3.56 ± 0.59 and 3.56 ± 0.83 respectively. These tests confirmed that the particle blocker is a viable method for blocking large particles from reaching within the cavity and onto the mirrors without degrading data. Further testing in long-term continuous deployments will verify the filters long-term ability to keep mirrors cleaner. Mud spatter and rain have been common issues which the particle filter shows promise in mitigating.

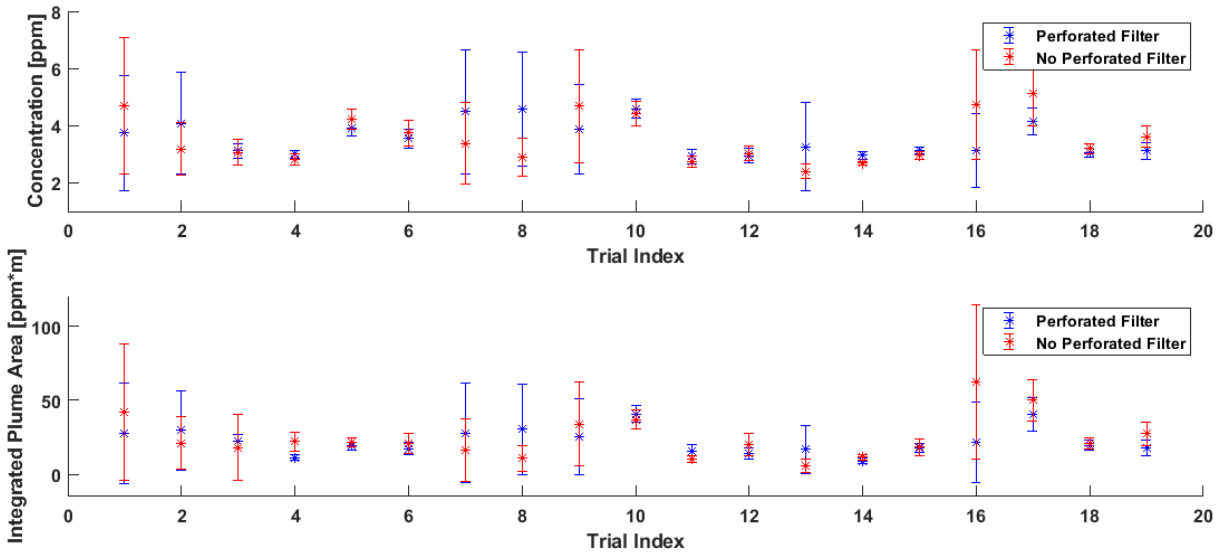

Figure 3.10: Plume peak and plume area data for trials done with (blue) and without (red) the use of the mechanical perforated particle filter. No significant difference between the methods over the trials is apparent.

3.1.5 Closed-path Configuration Field Tests

A negative aspect of the open-path design is the influence of aerosol particles on the signal due to Mie scattering[25]. Software and hardware have been developed in the past to mitigate this effect. Most notably, a software filter is used which filter's outliers within section bins in the spectrum[25]. Figure 3.11 shows an example of the raw data spectrum used for concentration fitting with a high level of aerosol noise. Extreme aerosol loading in the air can cause increases in Allan deviation and is difficult to prevent through the use of a software filter.

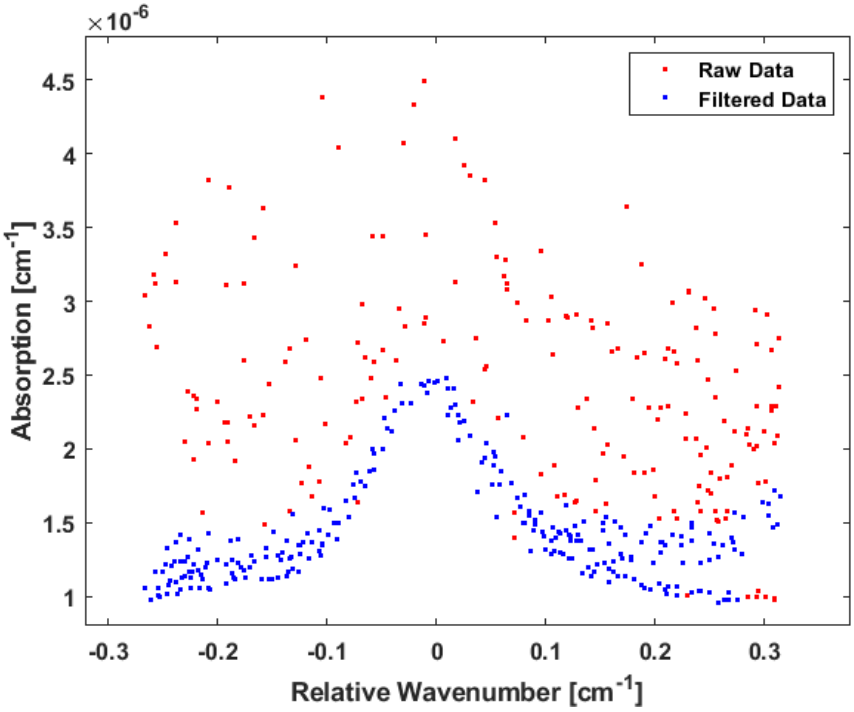

Figure 3.11: Example spectrum with heavy influence by aerosols (Mie scatter).

Within the lab, this is not an issue, but in varying field conditions, it can become troublesome. These effects in Colorado have been most notable while driving the sensor near traffic which produces large amounts of pollution. Over the course of this work, the open-path sensor data aerosol noise proved sufficiently low enough to yield adequate sensitivity (<35 ppb) most of the time, though occasionally the spectrum was perturbed by aerosol noise.

We therefore developed a new ("retro-fit") closed-path configuration in order to reduce overall aerosol noise, with also minimal increase in required sensor power draw. The design needed to come in a small enough package which was easy to install and remove when required. One of the main attributes of the open-path design which distinguishes it from closed-path sensors was its immediate response time to rapid methane spikes. Therefore, a design requirement was that the lag from inlet to cavity had to be less than 1 second to retain the time

response of the open path design. The lag (residence time) requirement for the pump flow was preliminarily calculated to be 0.3 seconds.

A 12-volt rotary vane pump (Thomas G08 50325) with a maximum flow rate of 15.5 l/min was used as the flow source for the setup. A particle filter (United Filtration Systems DIF-IN50) was used at the outlet of the pump to the closed cell. A smaller filter, which came with the pump, was used at the inlet to the pump. An enclosure was constructed to house all the components of the system. The components were chosen to be able to run on the 12-18 volts produced by vehicle batteries. Lastly, the flow cell was constructed out of two 8-inch NPT threaded PVC pipes, one NPT threaded PVC tee, and two NPT reducers which fit directly onto the rain blockers. The design of the closed cell is akin to that which was used for in-lab closed cell measurements described in Chapter 2. The material of the cell was changed to prevent the cell from vehicle induced excess vibrations which could cause clipping of the beam. A diagram and picture of the closed-path cell can be seen in Figure 3.12**.**

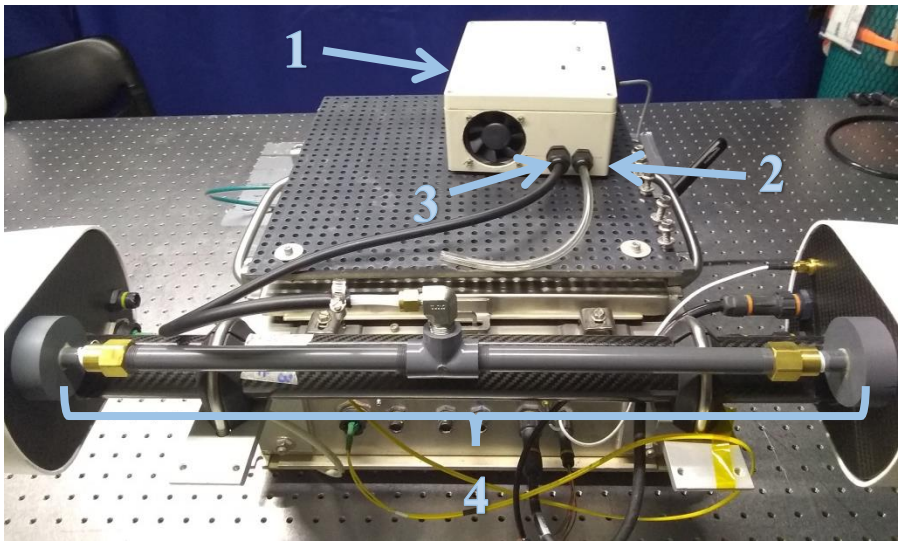

Figure 3.12: Closed-path configuration. 1: Pump and electronics enclosure. 2: Pump inlet. 3: Pump outlet to cavity. 4: Closed-path cavity cell.

Closed-path Response Time

The first concern when developing the closed-path configuration for the sensor was the possible lag in response time. The pump can supply a 15.5 l/min flow rate only when there is sufficiently low-pressure loss due to upstream components. Furthermore, the maximum continuous pressure loss that the pump is rated for is 0.3 bar which reduces the flow to ~13 l/min. Thus, the pressure loss due to the two filters should be ≤0.3 bar for a line which is 0.25 inches in diameter and ~80 inches in length from inlet to cavity in order to stay below a 0.3 second residence time. The final length of the line as seen in Figure 3.12 is ~60 inches. The pressure drop due to the line and filters combined was found to be ~0.03 bar which is an order of magnitude lower than the required 0.3 bar and therefore negligible.

Live testing was done to verify the closed-path's suitable response time. The schematic for the first latency test is shown in Figure 3.13**.** In Figure 3.13, Sensor 6 employs the closed-path configuration from Figure 3.12 with the pump. Sensor 7 utilizes the closed-path configuration described in Chapter 2.

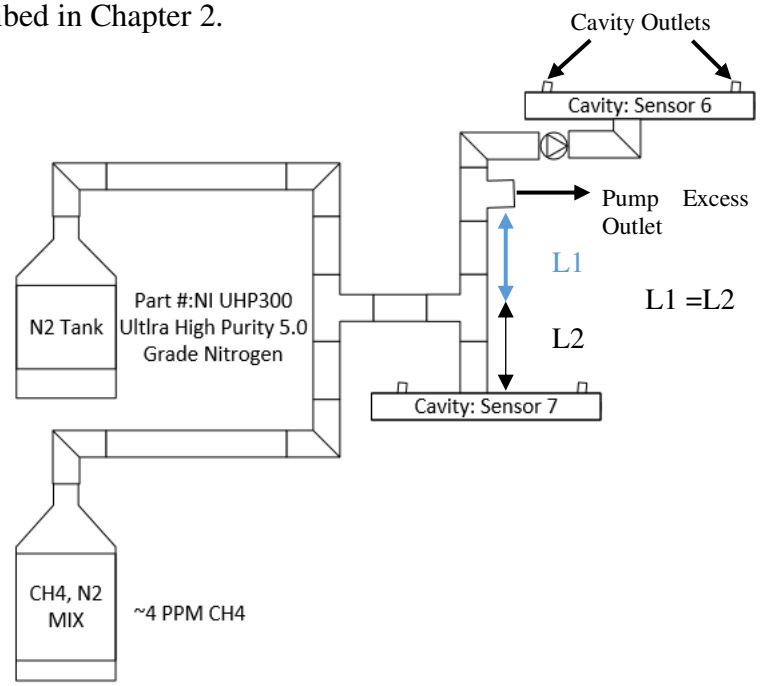

Figure 3.13: Schematic for closed-path latency tests.

The first test verified that the latency caused by the pump was on the order of 1 s. Because our sensor takes data at one second intervals, any latency below this would be immeasurable. The tank of CH_4 was used to provide the increase in concentration, while the N_2 tank reduced it. The flow rate at which the CH_4 was provided was set to be larger than that of the inlet of the pump to ensure that the dose would reach the pump inlet and the cavity of Sensor 7 at the same time. The results were as expected and a latency larger than 1 s was not observed.

The second group of tests verified that the closed-path configuration would not have a noticeable latency when detecting plumes in the field as has been seen when comparing to the Picarro in Figure 3.14. The first step of this test was done within the lab using a fan as a wind source and a tank of 250 ppm CH_4 as the leak source. The inlet to the closed-path sensor was placed as close to the open-path cavity as possible.

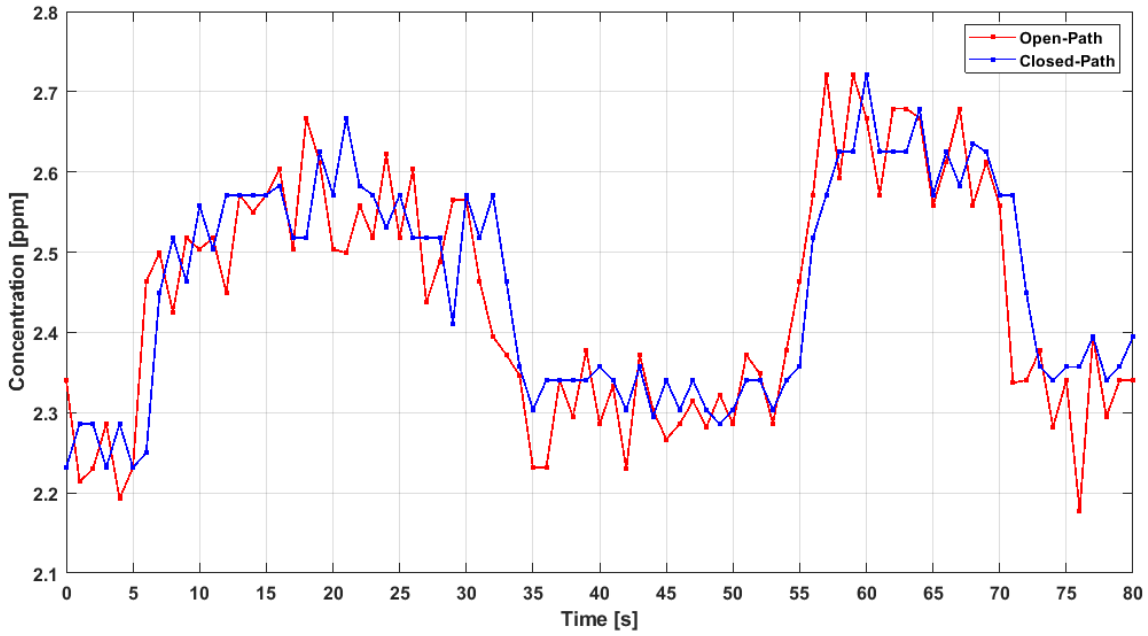

Figure 3.14: In lab latency test results showing a negligible (<1 s) measurement time lag caused by closed-path configuration.

The lag shown in Figure 3.16 was deduced to be less than or equal to 1 s (due to the inability to measure shorter lag time). This measurement solidifies further the effectiveness of the pump system. Live controlled release tests were then conducted to reinforce the previous findings. Both the open-path and closed-path sensors were mounted on the roof of a Ford Expedition. The proximity of the inlet of the closed-path to the open cavity was less than 6 in. Again, the latency between methods is negligible, and the closed-path configuration has fundamentally the same time response as an open-path sensor to one second precision.

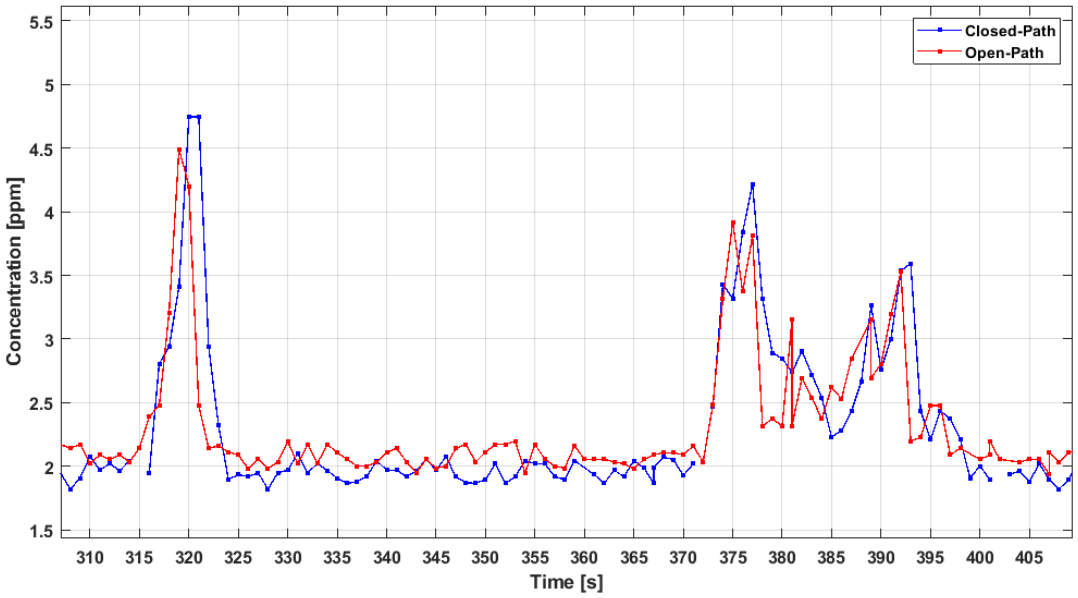

Figure 3.15: Controlled release test results showing closed-path and open-path response time in the field. Once again lag time was found to be <1 s.

Generally good 1:1 agreement between the two methods can be seen throughout the results of the response time tests seen in both Figure 3.14 and Figure 3.15. Controlled release tests also gave the ability to compare plume peak concentration and plume area with respect to the open-path and the closed-path sensor which also exhibited close agreement in the field.

Overall, these results bode well for future deployments of sensors utilizing the semi closed-path configuration introduced in this chapter. This configuration can reduce noise caused

by micron sized particles without reducing the time response of the sensor. Furthermore, not many components are needed to convert the sensor into its closed-path configuration.

Closed-path Sensitivity

Before the full deployment of the closed-path configuration, testing of sensitivity in a multitude of conditions was needed. The stability of the closed-path sensor in the field is hypothesized to be better than that of the open-path due to the reduction of influence from aerosol particles. Within the lab the stability of both sensors was found to be comparable since the software aerosol filter was enough to neglect the effects of aerosols. Figure 3.16 shows example spectra from within the lab with and without the use of the closed-path configuration.

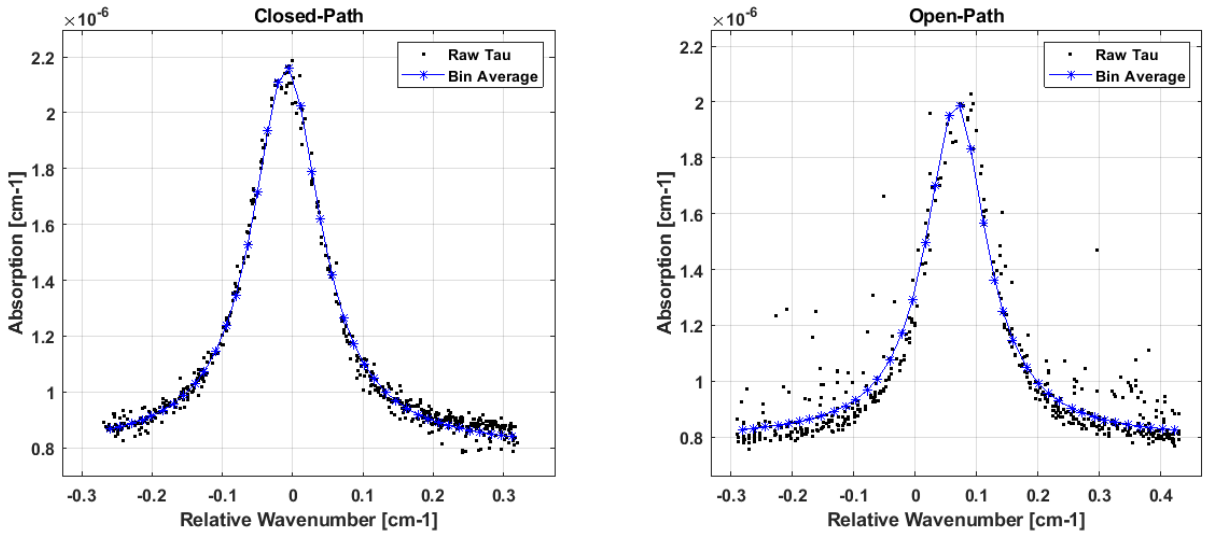

Figure 3.16: Absorption spectra with/without use of mobile closed cell within the lab.

The closed-path demonstrated a sensitivity of <31 ppb for a variety of conditions (e.g. within lab ~14 ppb, outside ambient ~23 ppb, driving in traffic ~31 ppb). The closed-path sensitivity was comparable (rather than better) to that of the open-path sensor in these conditions due to thermal effects caused by the pump configuration which negatively affected sensitivity.

As described in previous chapters, thermal sensitivity of the sensor is one of the main issues addressed in its current development. Sensitivity tended to drop significantly when the pump ran for long periods of time. Degradation in sensitivity was caused by the increasing temperature of the pump which functioned as a heater to the air introduced into the cavity. The heated air in turn heated the cell components as well as optical components which began to misalign the cavity. The much lower CTE of the PVC cell as well as the new structural connection between the two heads also contributed to reduction in performance due to the closed-path configuration. The overall performance dependence on high temperatures was increased due to the new mechanical structure of the closed cell.

Two solutions to this problem were considered. Increasing the length of tubing from the pump to the cell helped reduce the overall temperature of the air before it reached the cavity but had the downside of possibly increasing lag time. Heat sinking the pump more effectively also produced better results. To produce better heat dissipation from the pump, a specialized heat sink shown in Figure 3.17 was designed. The machining of the heat sink was done by The Rapid Prototyping and Applied Engineering Lab.

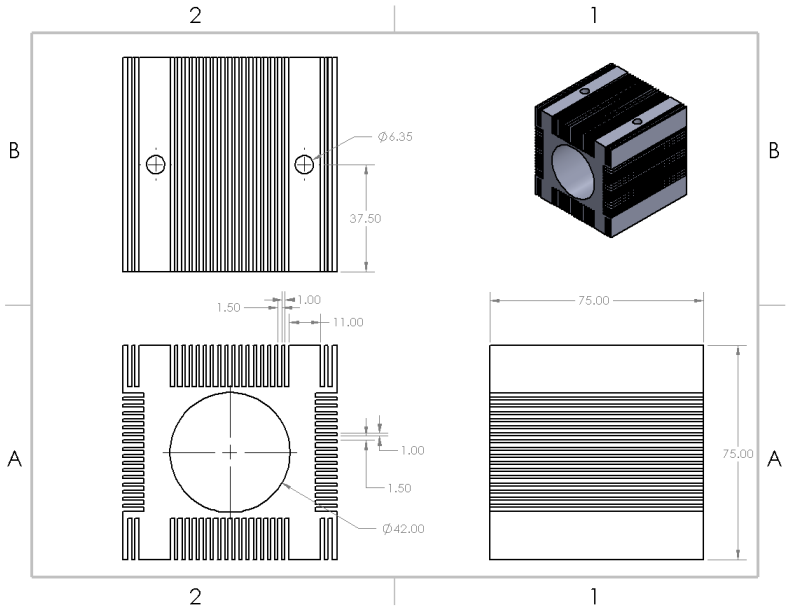

Figure 3.17: Heat sink designed to reduce heat produced by pump.

Lab measurements before heat sinking saw the Allan deviation increase by 30 ppb, the trigger level decrease by 0.1 volts, and the hottest temperature within the pump enclosure reach 41°C. This massive decrease in sensitivity would greatly influence the ability to detect trace concentration levels in the field. The heat sink effectively reduced the Allan deviation increase to 4 ppb, the trigger reduction to 0.04 volts, and the hottest temperature within the enclosure to 34°C. Overall the heat sink proved to be an effective method for restricting the negative effects produced by the heat of the pump. More work is still needed to reduce this effect further, and will be addressed in the future work section of this thesis

CHAPTER 4: UAV Deployed Field Tests

The sensor's design was developed with the idea of dual deployment on automobile and small unmanned aerial vehicles (UAVs). Taking vertical profiles along with horizontal ground measurements can greatly improve the accuracy of plume dispersion modeling. The vertical profiles of the plume can be modeled in the same way that the horizontal profile is modeled. Figure 4.1 below demonstrates a vertical profile of a Gaussian plume model. Emission detection through various platforms is attractive because it can provide flexible coverage of leak sources. The low operation costs and generally low regulation of UAV systems also make it a desirable platform for methane detection[24].

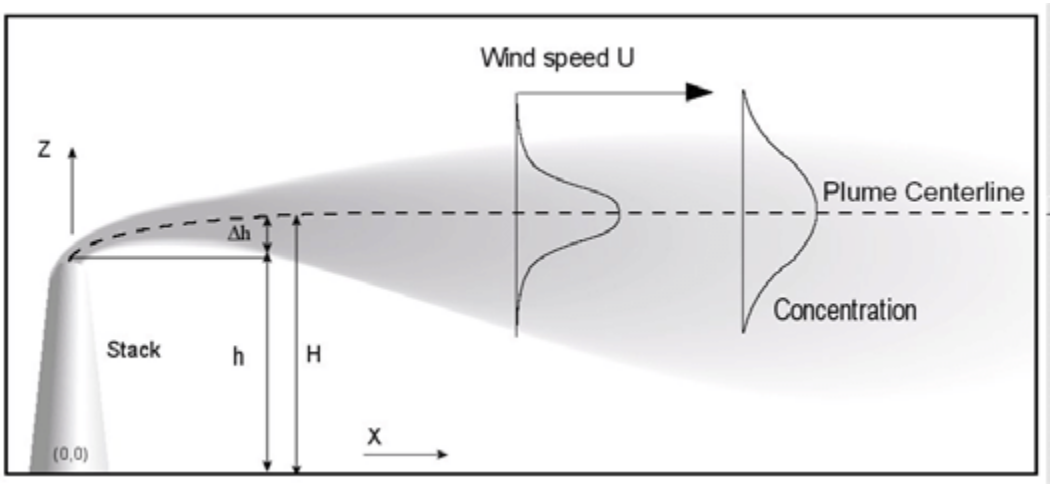

Figure 4.1: Gaussian Plume for air dispersion model[47].

4.1 Fixed Wing Aircraft

Previous work[25] described the process of mounting the sensor on a fixed wing Telemaster hobby plane with a payload capacity of 7.9 kg. The fixed wing platform was first chosen because of its high payload capacity with respect to other formats. A higher payload capacity allowed for the mounting of two sensors (the methane sensor described in this thesis and an open-path WMS ammonia sensor). The goal for the methane/ammonia coupling was to measure ammonia

deposition rates as is described in Shadman's Ph.D. dissertation[48]. The fixed wing aircraft made fitting two sensors more feasible.

The sensors were flown successfully on the fixed wing a few times, but controlled releases to measure the full extent of the platform were never completed. The fixed wing platform gave way to a few issues that made testing difficult. Take-off and landing required a runway which can be difficult in oil and gas locations. Uncertainty in landing also caused concerns of damaging the sensors. More work is still being done in this respect.

Data from these flights successfully displayed the capabilities of the open-path sensor to withstand take-off, in flight, and landing conditions produced by the fixed wing aircraft. The Allan deviation for flights were in the range of ~20 ppb demonstrating the robust capabilities of the sensor. Ingestion rates also remained on average at 500 τ/s and never went below 400 τ/s. Figure 4.2 below demonstrates the stability of the sensor while in-flight at varying speeds.

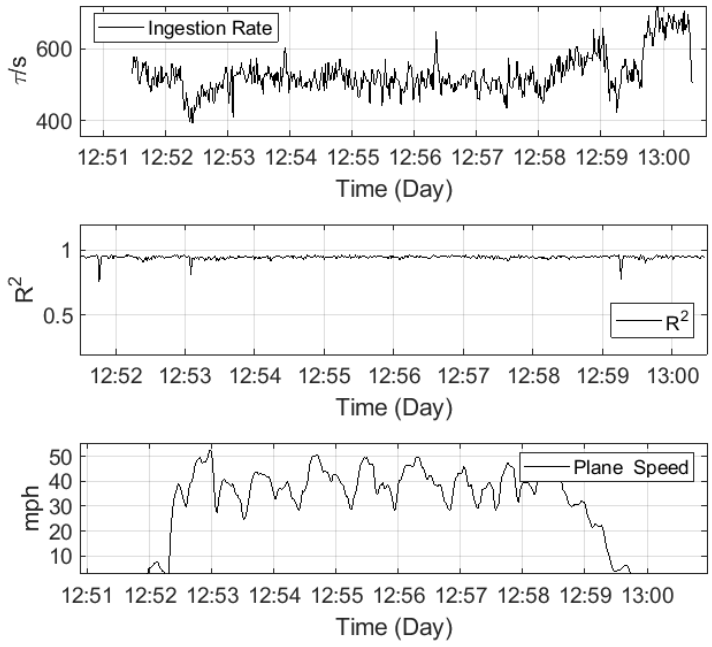

Figure 4.2: Top: Ingestion rate. Middle: R^2 for each fit, Bottom: Sensor speed.

4.2 Hexacopter

Collaboration with the CSU Drone Center led to the use of a vertical take-off and landing (VTOL) hexacopter (DJI Matrice 600). The hexacopter was introduced into the project for UAV deployment of the methane sensor specifically with the focus of oil and gas leak detection. The VTOL hexacopter demonstrated a multitude of advantages over the fixed wing aircraft that made acquiring flight data much easier. The ability of the hexacopter to operate near ground level, scale up in increments, hover, and operate at variable flight speeds produced an advantage for attempting to map the vertical profile of the plumes. Relatively low speeds compared to the fixed wing aircraft were also possible. Lastly, complex flight paths which mirror vehicle paths, could lend to better data collection overall. Flexibility in flights can be used for more accurate localization and quantification by performing a series of transects in varying patterns (e.g. spiral, staircase patterns etc.) of methane plumes downwind of emission sources.

The main concern of employing the Matrice was whether propeller wash would prevent proper air flow into the open cavity and prevent (or distort) detection of plumes. Work has also been published demonstrating various regions where propeller wash is negligible but on considerably smaller four propeller drones[49]. Since the optical head of the sensor is too large to mount 18 inches away from the body (the length of the propeller arms) it was decided to mount it directly beneath and as close to the body of the Matrice as possible.

4.2.1 Mounting and Integration

The maximum load capacity of the Matrice is 6 kg, but to keep flight times to a maximum, the payload weight was reduced to ~4.1 kg. The payload consisted of three main components: the optical head (Figure 4.3, left), the electronics enclosure (Figure 4.3, right), and an thin AOM mounting plate (not pictured). The AOM plate was not included within the

electronics enclosure due to a design change from free-space to fiber-coupled AOM. Note that the configuration used for the UAV is substantially smaller and lighter than that deployed on automobiles. The compact electronics enclosure for UAV payloads has approximate dimensions of 29 cm x 14 cm x 8 cm, with mass of 1.4 kg. The optical head used for UAV deployments has a ~40% lower mass (~2.0 kg) than its automobile deployed counterpart. The remaining 0.7 kg is due to mounting hardware and the AOM plate.

The electronics enclosure was attached to the body of the Matrice by use of Z15 series gimbal mounting connectors which attached to the enclosure by use of a lightweight plastic plate (high-density polyethylene, HDPE) with segments deliberately cut out to reduce weight but maintain structural integrity. Two mounting brackets machined out of ABS plastic attach the optical head to the electronics enclosure. The AOM plate was mounted directly on top of the plastic plate. Wires connecting between components were shortened as much as possible to reduce weight. Temperature and pressure probes, as well as the heater system, were also removed to reduce weight. Temperature and pressure data taken from ground-based sensors were used to post process data collected by the UAV system. The final mounting configuration can be seen in Figure 4.4

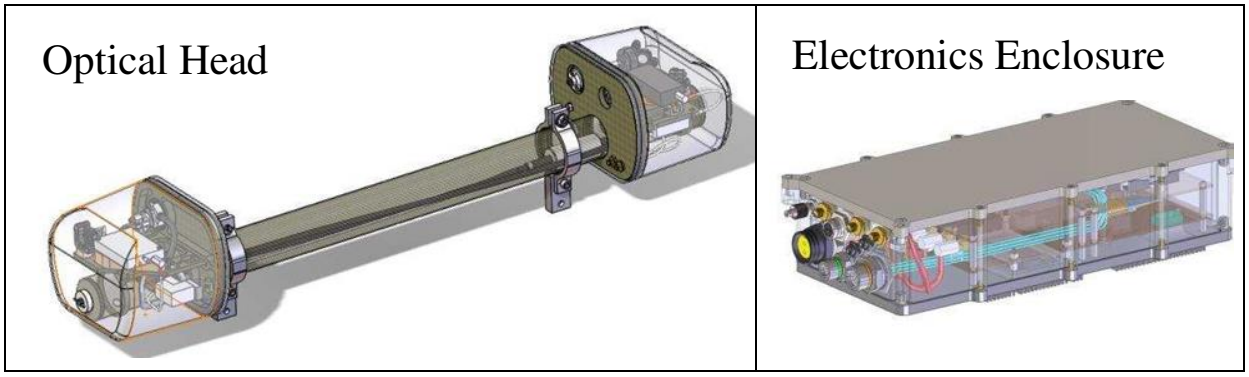

Figure 4.3: Components of UAV sensor payload

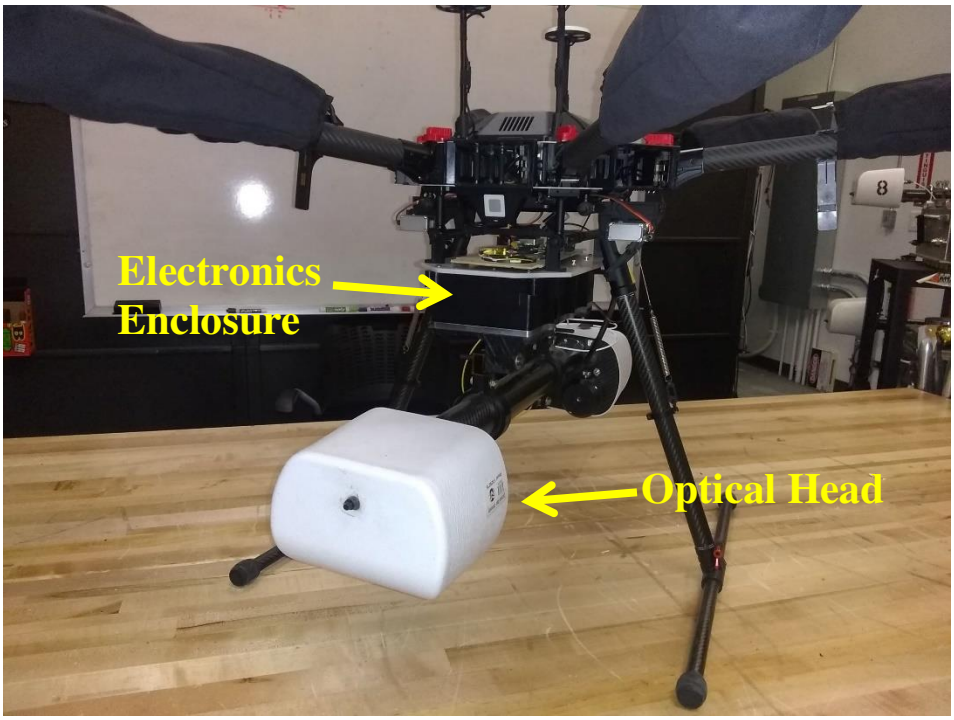

Figure 4.4: Fully integrated UAV payload design. All components used in release measurements are shown.

18 volts directly from the UAVs battery system (DJI TB47S) were used to power the sensor (~12 watts). Powering the sensor directly from the drone reduced the weight by bypassing individual battery systems for the sensor but at the cost of reducing overall flight times due to the higher power draw from the UAV batteries. Multiple sets of UAV batteries were used for each field test to allow for multiple flights per day. Flights were done at Christman Field with the same controlled release setup outlined in previous sections.

The mounting of the sensor did not noticeably affect the aerodynamics or control of the UAV. The sensor's high detection sensitivity during hexacopter flights also demonstrates the sensor's robust mechanical structure that is insensitive to vibrations and movements produced in flight. Allan deviation analysis revealed sensitivity as low as 17 ppb and an average sensitivity of 27 ppb. Degradation in flight sensitivity is attributed primarily to Mie scattering and thermal effects on cavity alignment. Over 13 flights, the reflectivity of the mirrors stayed well above the

required level and little to no realignments were needed. The sensor's performance over the course of the flights confirmed the possibility of use of the sensor in a UAV system that many commercial instruments are not capable of.

4.2.2 Detection

Methane plume detection under the influence of the UAV propeller wash was a main concern when conducting the first flight field tests. The goal of the first flight was to successfully detect plumes using the UAV system and make a first level assessment of the inflight detection capabilities. The vehicle mounted open-path sensor monitored ground level plumes as a reference. Throughout all tests, the UAV pilot, a CSU student, Jared Ham, attempted to fly the UAV directly above the ground-based sensor mounted on a vehicle.

The first group of flights conducted on June 8th, 2019, were successful in detecting plumes at various heights and distances from the leak location. Four flights were conducted on this day, each with varying altitude patterns. The leak rate was set to ~45 l/min (~0.5 g/s). The success of the first test supported the feasibility of detecting plumes with the current mounting system. Reproducibility of detection over a cyclical route at different altitudes and the close spatial agreement between plumes from the UAV and ground sensors also support the feasibility of using the closed-path sensor on a UAV for methane detection. Spatial agreement of plumes for the UAV and ground sensor can be seen in Figure 4.5.

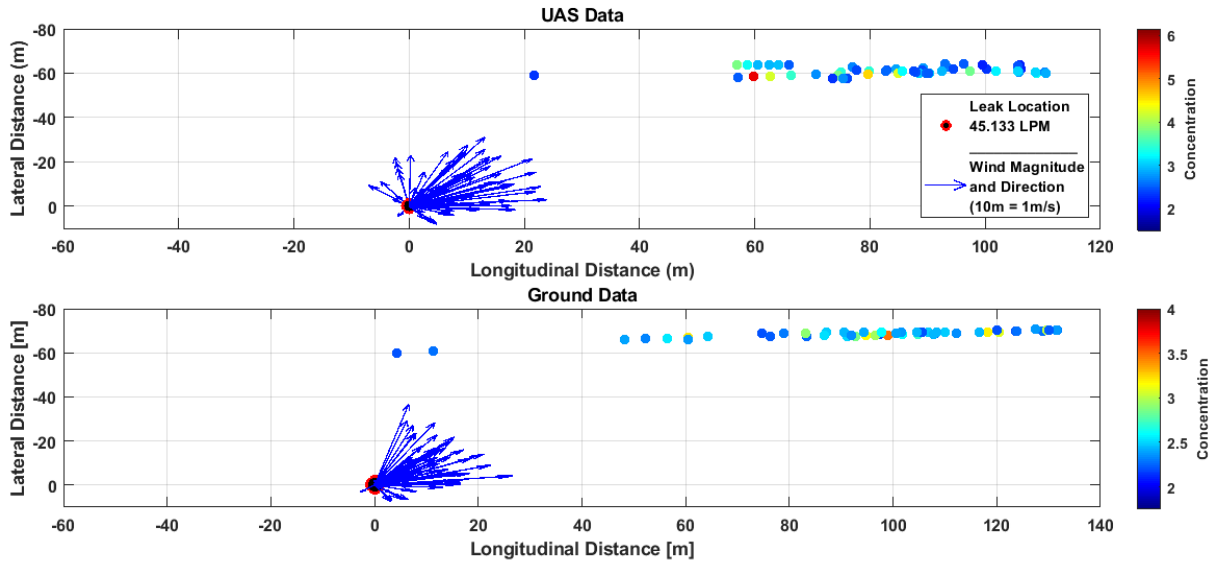

Figure 4.5: Overhead view of UAS data (Top), and ground sensor data (Bottom). Close spatial agreement strengthens the use of UAV system as a method for mapping the vertical profile of plumes.

More analysis on the possible effects of the UAV propellers on plume detection was done for various flights. Truck reading comparisons to UAV readings at similar height gave a better idea of these effects by verifying plume readings between the UAV and ground sensor, but more robust tests are needed to make any solidified conclusions. The data over four flights show an expected trend pointing to accurate mapping of the plume.

An emphasis during the next tests was put on creating a 3-dimensional vertical map of the plume as seen in the dispersion Figure 4.1. Vertical profile data of plume dispersion can greatly increase the ability to localize and quantify leak sources. After the first day of flights, more consideration was put on accurately mapping the plume. The 3-dimensional structure of plumes and varying flight patterns is illustrated in Figure 4.6. Spatial agreement of plume measurements between the UAV system and the ground vehicles system illustrates the overall reliability of 3-dimensional plume mapping through this technique.

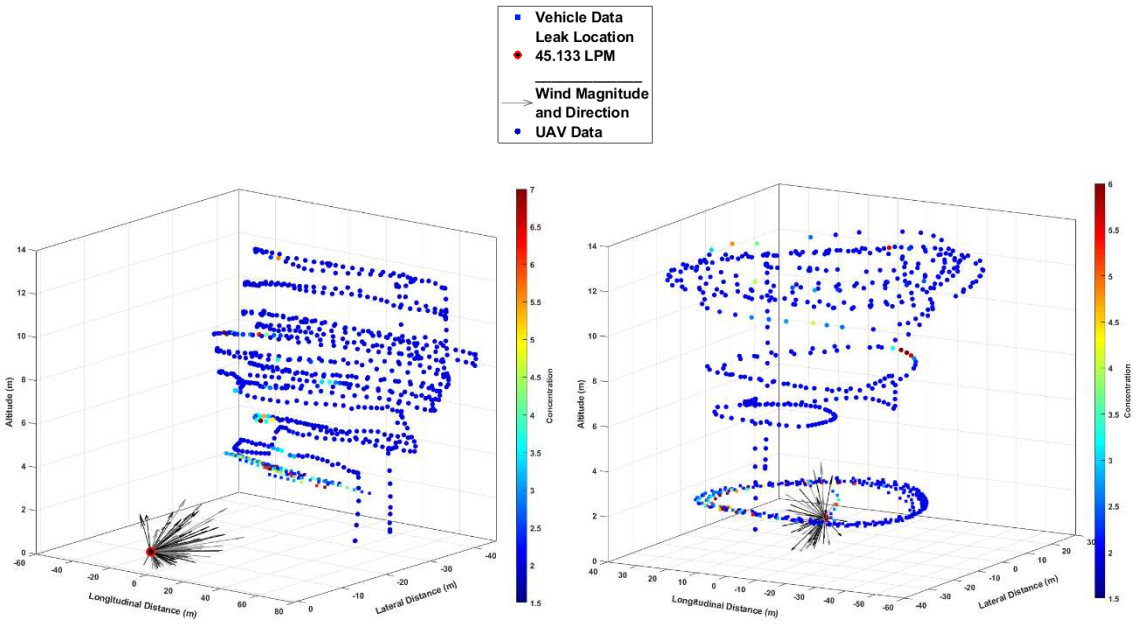

Figure 4.6: Plume methane concentration data from UAV system from two flights with varying flight patterns.

Accurately mapping the plume requires multiple horizontal transects at a given distance and height from the source starting as low to the ground sensor as possible and slowly moving up in altitude until there are no more elevated readings. This can help estimate the bounds of the plume in the vertical and horizontal directions as modeled in a Gaussian distribution in Figure 4.1. The ground sensor was mounted on the roof of a Ford Expedition which is approximately 2 meters from the ground. The UAV could only be flown as low as ~4 meters from the ground due to safety precautions.

Figure 4.7 shows an attempt at capturing the full vertical extent of the plume, but short flight times prevented the continued increase in altitude. Elevated plume readings from the UAV were measured at altitudes of ~25 meters through a consistent vertical rise flight path. Downwind distances ranged from 75 to 150 meters. The methane release had a mass flow of 0.5 g/s with an average wind speed of ~1.5 m/s. Short flight times greatly reduced the ability to gather large amounts of data at multiple altitudes for long periods of time over single flights.

Flight times coupled with instability in the wind direction gave rise to plume mapping complications as routes around the emission source became more sporadic with the wind.

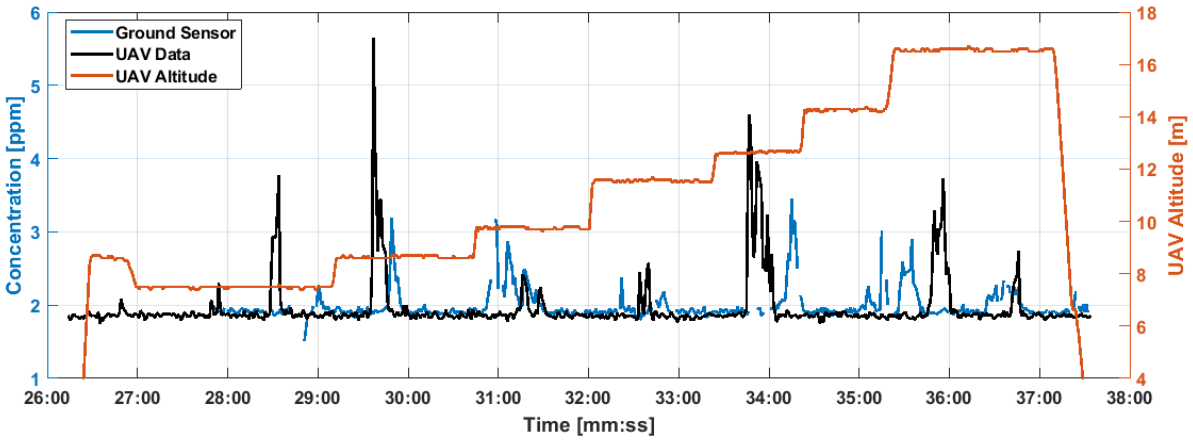

Figure 4.7: Plume concentration measurements for UAV (black), and ground sensor (blue). Altitude steps were taken to attempt to map the vertical extent of the plume (orange).

Figure 4.8 demonstrates specific plume transects at various heights captured by the UAV and ground systems for two specific flights at a controlled release rate of 0.5 g/s methane . An increase in size of the plume can be seen in both 06/08/19 data as well as 06/15/19 data. The data at an altitude of 2 meters were taken with an automobile mounted sensor. The very weak amplitude of the plume at 24.9 meters altitude indicates the possible transect over the tope edge of the plume.

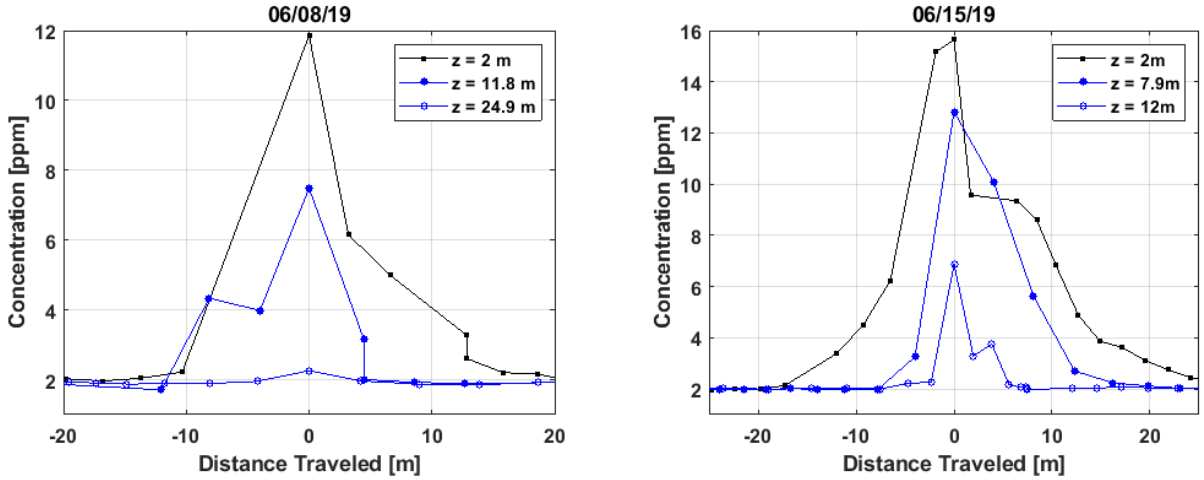

Figure 4.8: Plume concentration values over distance traveled for various altitudes for the UAV and ground sensor over four test days.

While more work on quantification and localization is needed to deduce the improvement of using a UAS coupled with the ground sensor, through this work, the capabilities of the sensor for UAV deployment were clearly demonstrated. Plume measurements were recorded at various heights and sensitivity was comparable to ground-based deployment. UAV flights encompass the capabilities of the sensor's scalability for surveillance over broad regions.

CHAPTER 5: Conclusions

The global impact produced by anthropogenic methane emissions into the lower atmosphere frames the importance of this work. The copious amounts of methane emissions from the oil and gas industry, as well the lack of sensitive high-throughput mobile detection systems also contribute to the significance of research in this area. This work demonstrates the trace methane detection capabilities of an open-path cavity ring-down based sensor developed primarily for use in oil and gas applications. The feasibility of deploying the sensor in a variety of mobile platforms is also analyzed. The theory describing the method for detection is outlined in Chapter 1, along with a description of the unique attributes employed by the sensor in this thesis. The verification and improvement of the sensor's sensitivity and performance in various non-mobile conditions are demonstrated in Chapter 2. Chapter 3 illustrates the performance of the sensor in field tests, as well as modifications made to the sensor for improving its performance in various conditions. In Chapter 4, the sensor's capabilities for deployment on UAV systems is investigated. A summary of the findings presented in this thesis, as well as future work to further improve this sensor system, are presented in the next sections.

5.1 Summary

The sensor's accuracy in measuring methane, detection capabilities in various weather conditions, and software capabilities are described in Chapter 2. Sensor accuracy was found to strongly agree with reference CH_4 tanks to less than 0.093 ppm. Its accuracy compared to a commercial gas analyzer also shows close agreement between the two as seen in Figure 2.5. Sensitivity of the sensor in laboratory conditions is well within the range for plume detection at 10-20 ppb. The dependence of temperature on the optical-based sensors is apparent; therefore, a heating system was designed to mitigate the effects of low temperatures on alignment. The

heating system outlined in Chapter 2 shows sensor improvement under temperature conditions as low as 0°C as well as improvements in harsh conditions over long-term (70 day) stationary deployments.

Controlled release measurements were conducted and outlined in Chapter 3. Tests were constructed to quantify the sensor's sensitivity and detection abilities over oil and gas simulated leak point sources as a starting point for quantification and localization. Detection trends show a close agreement to Gaussian plume dispersion models of concentration as a function of distance from the source (Figure 3.6). Comparisons with commercial instruments outlined a key issue demonstrated by the open-path sensors which led to efforts to resolve the underestimation of plume concentration and area. Factors which affect this discrepancy have been found to be sampling time, and software fitting success. These issues have been addressed and moderated through this work. Emphasis was put on solutions involving software fitting algorithms.

A mechanical perforated particle filter was also designed and tested to gauge the possibility of its long-term use to prevent data degradation due to large particle deposition on mirrors. The viability of its use was demonstrated, and it was shown that it negligibly affects plume detection as well as sensitivity over varying conditions (Figure 3.12, Table 3.1). Lastly, to address micron-sized particles, the open-path cavity was converted into a closed-path cavity. The closed-path cavity allowed filtration of the air introduced into the cavity which reduced particle loading within the optical cavity. The sensor's time response was shown to be less than 1 second enabling an effective temporal response even with a closed cavity. The sensitivity of the closed-path configuration was <31 ppb and further improvements to the system should increase the sensitivity. The detection abilities of the closed-path also show the feasibility of its use in the field.

Chapter 4 sees the modification of the sensor for deployment on an unmanned aerial vehicle. This thesis demonstrates the first use of a lightweight CRDS sensor integrated onto two UAV platforms. The feasibility of this modification onto a fixed wing aircraft is described and shows no inflight degradation in signal. The sensor was then mounted on a VTOL hexacopter to take controlled release data. Sensitivity (~20 ppb) and spatial plume detection were consistent with ground readings expressing UAS deployment feasibility.

5.2 Future Work

Future work of the sensor should focus on six main aspects: reduction of sensor thermal dependence; modification of sensor design to encourage long-term stability; further modification to the fitting algorithm; characterization of controlled release detection limits as a function of distance for small leaks on the order of 2 l/min; continued modification and characterization of the closed-path configuration; and increase data collection with UAV.

Thermal dependence of the sensor has been a consistent issue faced during this work. Better understanding of individual component's role in thermal dependence can lead to a better overall design of the sensor. Modifications to the heating system and insulation can also lead to better mitigation of this issue. Long-term mirror cleanliness should also be addressed through either redesign of mirror placement or further testing of the perforated particle filter to assess its effects on mirror cleanliness.

Current work is being done to modify the fitting algorithm to address plume underestimation by the open-path sensor. Binning algorithms have shown promise in being much better at quantifying large concentrations, but more data and comparisons with commercial sensors is required to verify their functionality in controlled release field tests. The possibility of

modifying the sampling rate to 3 Hz while processing in real-time should also be studied since data suggest it could assist in more accurate measurements.

More field tests with controlled release are also needed to better quantify the limits of detection of the sensor at lower leak rates. The gas industry is interested in detecting leaks as low as 0.05 l/min which is two orders of magnitude lower than the lowest leak rate tested in this work. The distance from the source needed to detect leaks of this order should be quantified to assess overall performance. Tests of this kind with the closed-path configuration should also be done to characterize whether a closed-path cell can detect comparable sized leaks as well as or better than the open-path. The closed-path configuration also tends to have a larger temperature dependence than open-path due to larger thermal warping of the entire optical head. Precise characterization of this dependence as well as modifications to moderate it would give better overall sensor capabilities.

Lastly, as stated in Chapter 4, more UAV flights are necessary to accurately describe the extent for which the propeller wash affects readings and the extent at which 3-dimensional vertical mapping of the plume is possible. Further work also includes analysis of the data to assess the ability to accurately quantify and locate methane emissions. Work is currently being done in this regard and shows promise in the sensor's ability to provide data which can be turned around to calculate the location and emission rate of an unknown source. More attempts at localization and quantification from the data provided by this thesis should be done to assess the overall needed improvements of the sensor's detection ability.

BIBLIOGRAPHY

1. Pachauri, R. K. & Meyer, L. IPCC, 2014: Climate Change 2014: Synthesis Report. Contribution of Working Groups I, II and III to the Fifth Assessment Report of the Intergovernmental Panel on Climate Change. *IPCC* (2014).

2. Pinault, J. L. Anthropogenic and natural radiative forcing: Positive feedbacks. *J. Mar. Sci. Eng.* **6**, (2018).

3. Mckee, D. Tropospheric ozone: human health and agricultural impacts. in *Choice Reviews Online* vol. 32 32-2752-32–2752 (1995).

4. United States Environmental Protection Agency. EPA 430-R-19-001: Inventory of U.S. Greenhouse Gas Emissions and Sinks 1990-2017. (2019).

5. Alvarez, R. A. *et al.* Assessment of methane emissions from the U.S. oil and gas supply chain. *Science (80-.).* **361**, 186–188 (2018).

6. Saunois, M. *et al.* The global methane budget 2000-2012. *Earth Syst. Sci. Data* **8**, 697–751 (2016).

7. Chemical Composition of Natural Gas - Union Gas. https://www.uniongas.com/about-us/about-natural-gas/chemical-composition-of-natural-gas (2019).

8. Lee, S. Y. & Holder, G. D. Methane hydrates potential as a future energy source. *Fuel Process. Technol.* **71**, 181–186 (2001).

9. U.S. EIA. Annual Energy Outlook 2019 with projections to 2050. *Annu. Energy Outlook 2019 with Proj. to 2050* **44**, 1–64 (2019).

10. Howarth, R. W. Ideas and perspectives: Is shale gas a major driver of recent increase in global atmospheric methane? *Biogeosciences* **16**, 3033–3046 (2019).

11. Barrels, B. B. L. Colorado Oil and Gas Conservation Commission Spill Analysis by Year 1999 – 2 nd Qtr 2019. 2019 (2019).

12. Oil and Gas Climate Initiative. https://oilandgasclimateinitiative.com/ (2019).

13. Ravikumar, A. P., Wang, J. & Brandt, A. R. Are Optical Gas Imaging Technologies Effective for Methane Leak Detection? *Environ. Sci. Technol.* **51**, 718–724 (2017).

14. Coburn, S. *et al.* Regional trace-gas source attribution using a field-deployed dual frequency comb spectrometer. *Optica* **5**, 320 (2018).

15. Thorpe, A. K. *et al.* The Airborne Methane Plume Spectrometer (AMPS): Quantitative imaging of methane plumes in real time. *IEEE Aerosp. Conf. Proc.* **2016-June**, 1–14 (2016).

16. Kuai, L. *et al.* Characterization of anthropogenic methane plumes with the Hyperspectral Thermal Emission Spectrometer (HyTES): A retrieval method and error analysis. *Atmos. Meas. Tech.* **9**, 3165–3173 (2016).

17. Frankenberg, C. *et al.* Airborne methane remote measurements reveal heavytail flux distribution in Four Corners region. *Proc. Natl. Acad. Sci. U. S. A.* **113**, 9734–9739 (2016).

18. MethaneSAT. https://www.methanesat.org/about-methanesat/ (2019).

19. Propp, A. M., Benmerfui, J. S. & Turner, A. . MethaneSat: Detecting Methane Emissions in the Barnett Shale Region. **2017**, A32D-06 (2017).

20. Ravikumar, A. P. *et al.* 'Good versus Good Enough?' Empirical Tests of Methane Leak Detection Sensitivity of a Commercial Infrared Camera. *Environ. Sci. Technol.* **52**, 2368–2374 (2018).

21. FLIR. Optical gas imaging. *Pollut. Eng.* **46**, (2014).

22. Crosson, E. R. A cavity ring-down analyzer for measuring atmospheric levels of methane, carbon dioxide, and water vapor. *Appl. Phys. B Lasers Opt.* **92**, 403–408 (2008).

23. Smith, B. J., John, G., Christensen, L. E. & Chen, Y. Fugitive methane leak detection using sUAS and miniature laser spectrometer payload: System, application and groundtruthing tests. *2017 Int. Conf. Unmanned Aircr. Syst. ICUAS 2017* 369–374 (2017) doi:10.1109/ICUAS.2017.7991403.

24. Golston, L. M. *et al.* Lightweight mid-infrared methane sensor for unmanned aerial systems. *Appl. Phys. B Lasers Opt.* **123**, (2017).

25. Mchale, L. DEVELOPMENT OF MOBILE OPEN-PATH CAVITY RING-DOWN SPECTROMETER FOR MEASUREMENT OF TRACE ATMOSPHERIC METHANE GAS. (Colorado State University, 2018).

26. Albertson, J. D. *et al.* A Mobile Sensing Approach for Regional Surveillance of Fugitive Methane Emissions in Oil and Gas Production. *Environ. Sci. Technol.* **50**, 2487–2497 (2016).

27. Mchale, L. E., Martinez, B., Miller, T. W. & Yalin, A. P. Open-path cavity ring-down methane sensor for mobile monitoring of natural gas emissions. *Opt. Express* **27**, 20084 (2019).

28. Dudek, J. B. *et al.* Trace moisture detection using continuous-wave cavity ring-down spectroscopy. *Anal. Chem.* **75**, 4599–4605 (2003).

29. McHale, L. E., Hecobian, A. & Yalin, A. P. Open-path cavity ring-down spectroscopy for trace gas measurements in ambient air. *Opt. Express* **24**, 5523 (2016).

30. Hill, C. HITRANonline. https://hitran.org/docs/definitions-and-units/.

31. Hanson, R. K., Spearrin, R. M. & Goldenstein, C. S. *Spectroscopy and optical diagnostics for gases*. *Spectroscopy and Optical Diagnostics for Gases* (2016). doi:10.1007/9783319232522.

32. Anthony E. Siegman. *Lasers*. (University Science Books, 1986).

33. Kogelnik, H. & Li, T. Laser Beams and Resonators. *Proc. IEEE* **54**, 1312–1329 (1966).

34. KoHse-HoingHaus, K. & Jeffries, J. B. *Applied combustion diagnostics*. *Combustion and Flame* (Taylor & Francis, 2002). doi:10.1016/s0010-2180(03)00044-0.

35. Nagourney, W. *Quantum Electronics for Atomic Physics*. (Oxford University Press Inc, 2014).

36. Gagliardi, G. & Loock, H. *Cavity-Enhanced Spectroscopy and Sensing*. (Springer, 2016).

37. Yalin, A. P., Surla, V., Butweiller, M. & Williams, J. D. Detection of sputtered metals with cavity ring-down spectroscopy. *Appl. Opt.* **44**, 6496–6505 (2005).

38. Werle, P., Mücke, R. & Slemr, F. The limits of signal averaging in atmospheric trace-gas monitoring by tunable diode-laser absorption spectroscopy (TDLAS). *Appl. Phys. B Photophysics Laser Chem.* **57**, 131–139 (1993).

39. Huang, H. & Lehmann, K. K. Long-term stability in continuous wave cavity ringdown spectroscopy experiments. *Appl. Opt.* **49**, 1378–1387 (2010).

40. Picarro. PICARRO G2203 Methane / Acetylene Analyzer. (2015).

41. Turner, B. D. *Workbook of Atmospheric Dispersion Estimates*. *U.S. Environmental Protection Agency, AP-26* (1970).

42. Baasel, W. D. A simple technique for determining the maximum ground level

concentration of an elevated gaseous release. *J. Air Pollut. Control Assoc.* **31**, 866–870 (1981).

43. Agency, E. P. *User's Guide For The Assessment System For Population Exposure Nationwide (Aspen, Version 1.1) Model*. (Enivornmental Protection Agency, 2000).

44. Arfire, A., Marjovi, A. & Martinoli, A. Mitigating Slow Dynamics of Low-Cost Chemical Sensors for Mobile Air Quality Monitoring Sensor Networks. *Proceeding EWSN '16 Proc. 2016 Int. Conf. Embed. Wirel. Syst. Networks* 159–167 (2016).

45. Lee, J. K., Christen, A., Ketler, R. & Nesic, Z. A mobile sensor network to map carbon dioxide emissions in urban environments. *Atmos. Meas. Tech.* **10**, 645–665 (2017).

46. Patel, P. Monitoring Methane. *ACS Cent. Sci.* **3**, 679–682 (2017).

47. Mohamed, A. ICFD11-EG-4006 Air Quality Assessment of West Port-Said Industrial Region , ICFD11-EG-4006. (2018).

48. Shadman, S. MEASUREMENT OF AMMONIA EMISSION FROM AGRICULTURAL SITES USING OPEN-PATH CAVITY RING-DOWN SPECTROSCOPY AND WAVELENGTH MODULATION SPECTROSCOPY BASED ANALYZERS. (Colorado State University, 2018).

49. Smith, B., John, G., Stark, B., Christensen, L. E. & Chen, Y. Q. Applicability of unmanned aerial systems for leak detection. *2016 Int. Conf. Unmanned Aircr. Syst. ICUAS 2016* 1220–1227 (2016) doi:10.1109/ICUAS.2016.7502635.

50. Sternberg, S. P. K. *Air Pollution: Engineering, Science and Policy*. (College Publishing, 2015).

APPENDIX A:

Key to Stability Classes[a]

Surface Wind Speed at 10 m (m/s)	Day			Night	
	Incoming Solar Radiation			Cloud Cover	
	Strong	Moderate	Slight	Thinly Overcast or ≥50% Clouds	Mostly Clear or ≤$\frac{3}{8}$ Clouds
<2	A	A–B	B	—	—
2–3	A–B	B	C	E	F
3–5	B	B–C	C	D	E
5–6	C	C–D	D	D	D
>6	C	D	D	D	D

[a]The neutral class, D, should be assumed for overcast conditions during day or night
Source: D. B. Turner *Workbook of Atmospheric Dispersion Estimates* Washington, D.C. HEW, 1969.

Figure A.1: Dispersion modeling stability class estimates[50].

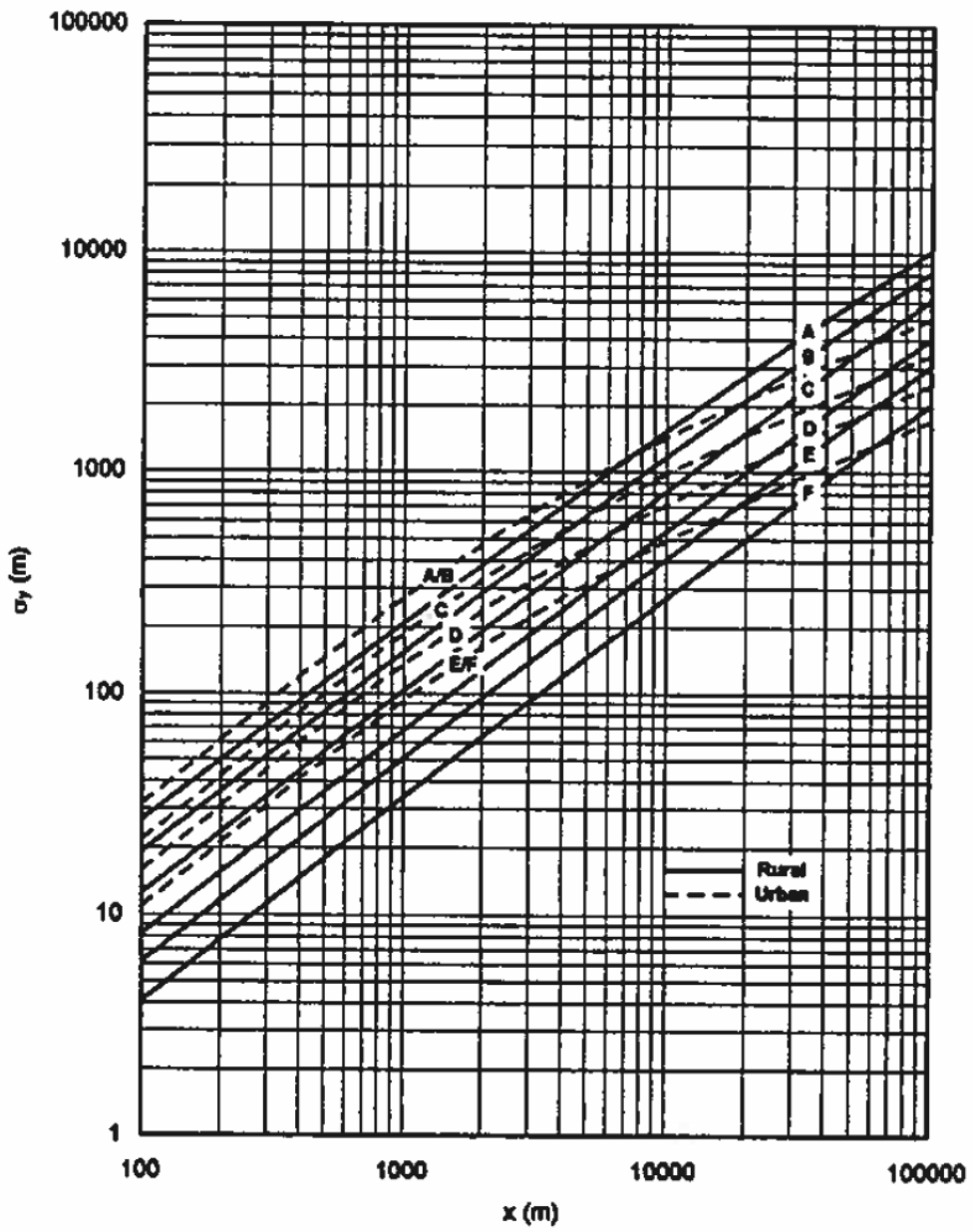

Figure A.2: Rural and urban horizontal dispersion coefficients as a function of stability category. (Graph Prepared by S.M. Claggett.)[50].

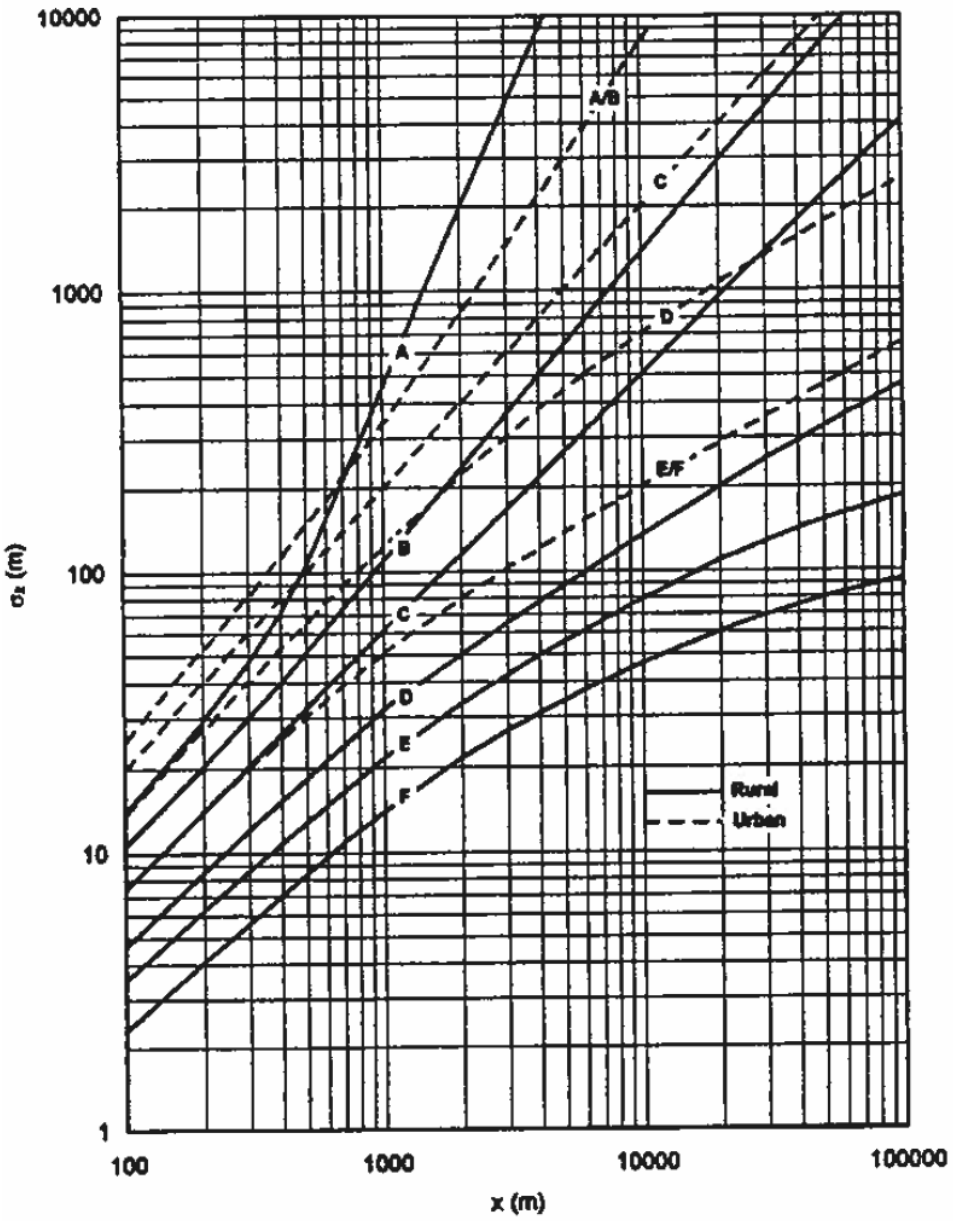

Figure A.3: Rural and urban vertical dispersion coefficients as a function of stability category. (Graph Prepared by S.M. Claggett.)[50].

Parameters Used to Calculate Pasquill-Gifford σ_y

Pasquill Stability Category	*c*	*d*
A	24.1670	2.5334
B	18.3330	1.8096
C	12.5000	1.0857
D	8.3330	0.72382
E	6.2500	0.54287
F	4.1667	0.36191

Figure A.4: Parameters used to calculate Pasquill-Gifford σ_y[50].

Parameters Used to Calculate Pasquill-Gifford σ_z

Pasquill Stability Category	x (km)	a	b
A*	<.10	122.800	0.94470
	0.10 – 0.15	158.080	1.05420
	0.16 – 0.20	170.220	1.09320
	0.21 – 0.25	179.520	1 12620
	0.26 – 0.30	217.410	1.26440
	0.31 – 0.40	258.890	1.40940
	0.41 – 0.50	346.750	1.72830
	0.51 – 3.11	453.850	2.11660
	>3.11	**	**
B*	<.20	90.673	0.93198
	0.21 – 0.40	98.483	0.98332
	>0.40	109.300	1.09710
C*	All	61.141	0.91465
D	<.30	34.459	0.86974
	0.31 – 1.00	32.093	0.81066
	1.01 – 3.00	32.093	0.64403
	3.01 – 10.00	33.504	0.60486
	10.01 – 30.00	36.650	0.56589
	>30.00	44.053	0.51179
E	< 10	24.260	0.83660
	.010 – 0.30	23.331	0.81956
	0.31 – 1.00	21.628	0.75660
	1.01 – 2.00	21.628	0.63077
	2.01 – 4.00	22.534	0.57154
	4.01 – 10.00	24.703	0.50527
	10.01 – 20.00	26.970	0.46713
	20.01 – 40.00	35.420	0.37615
	>40.00	47.618	0.29592
F	<.20	15.209	0.81558
	0.21 – 0.70	14.457	0.78407
	0.71 – 1.00	13.953	0.68465
	1.01 – 2.00	13.953	0.63227
	2.01 – 3.00	14.823	0.54503
	3.01 – 7.00	16.187	0.46490
	7.01 – 15.00	17.836	0.41507
	15.01 – 30.00	22.651	0.32681
	30.01 – 60.00	27.074	0.27436
	>60.00	34.219	0.21716

*If the calculated value of σ_z exceeds 5000 m, σ_z is set to 5000 m.
**σ_z is equal to 5000 m

Figure A.5: Parameters used to calculate Pasquill-Gifford σ_y[50].